Imaging of the Crust by Aftershocks of the 2000Western Tottori Prefecture Earthquake

著者	Shigeki NAKAGAWA
雑誌名	防災科学技術研究所　研究報告
巻	68
ページ	91-124
発行年	2005-09
URL	http://doi.org/10.24732/nied.00001165

Report of the National Research Institute for Earth Science and Disaster Prevention, No.68; September, 2005

Imaging of the Crust by Aftershocks of the 2000 Western Tottori Prefecture Earthquake

Shigeki NAKAGAWA

Solid Earth Research Group,
National Research Institute for Earth Science and Disaster Prevention, Japan
(*Current affiliation : Earthquake Research Institute, the University of Tokyo, Japan*)
nakagawa@eri.u-tokyo.ac.jp

Abstract

On October 6, 2000, a large earthquake occurred in the western part of Tottori Prefecture, Japan. To reveal the crustal structure in the fault area of this earthquake, we conducted aftershock observations using a multi-channel seismic array. Since natural earthquakes are not located on the surface of the earth, we developed a new method, the natural earthquake reflection profiling (NERP) method, to image the crust using natural earthquakes. We applied the NERP method to the aftershock data. The shallow area of the upper crust is reflective and the aftershock distribution is diffused three dimensionally in this area. Also found in this area are small less-reflective zones, in which brittle fracture does not occur and stable-slip deformation is dominant. It is possible that the stable-slip areas are distributed in the upper crust, which may contribute to the major characteristics of this earthquake.

Key words : Aftershock observation, Crustal structure, The 2000 Western Tottori Prefecture earthquake

1. Introduction

1.1 The 2000 Western Tottori Prefecture earthquake

On October 6, 2000, a large earthquake with a JMA magnitude of 7.3 occurred in the western Tottori Prefecture of Japan (**Fig. 1.1**).

Although the earthquake is a shallow large intra-island-arc type event, there are three characteristics different from common large earthquakes. This earthquake occurred in the area where (1) a surface rupture is not clearly observed, (2) no active faults are known, and (3) the maximum shear strain rate is lower than other areas (Geographical Survey Institute, 2001).

Fukuyama *et al*. (2003) relocated the aftershocks by the double-difference method, and they estimated very detailed fault structures activated by the main shock. They resolved 15 individual fault segments that were consistent with both the aftershock distribution and focal mechanism solutions (**Fig. 1.2**). Iwata and Sekiguchi (2001) analyzed the rupture process of the main shock, and they found that the slip occurred only in the southern part of the aftershock area.

The generation mechanism of such intra-island-arc earthquake is not clarified yet. The heterogeneous crustal structure is one of the key points to understand these earthquakes. To reveal the heterogeneous crustal structure in the fault area of this earthquake, many seismic observations or experiments were carried out.

1.1.1 Seismic reflection method (Fig. 1.3)

Kurashimo *et al*. (2001) conducted the seismic reflection survey using vibrators as a controlled seismic source. They deployed a CDP line located across the fault. They recognized reflected waves at two-way travel times (TWTs) of 3.5 and 6 s (**Fig. 1.4**).

Abe *et al*. (2001) also conducted a seismic reflection survey at other CDP lines across the fault. They recognized discontinuous reflectors converged wedge-wise with a depth at 3 s TWT, and they interpreted that these reflectors represent the characteristics of the flower structure. Moreover, they found that reflectors existed at a depth of 4 s TWT in the northern part of the fault, but no reflectors at the same depth in the southern part of the fault. This fact indicated that the crust is different in structure between that in the northern part and the southern part of the fault area.

Nishida *et al*. (2002) conducted a wide-angle seismic reflection survey using vibrators and dynamites as a controlled seismic source. They deployed a CDP line with a length of about 45 km located along the fault. In the southern part of the fault, a reflector was found at depths of 11 – 12 km (A). In the northern part of the fault, reflectors were found at depths of 13 – 14 km, and at a depth of about 27 km (corresponding to the Moho discontinuity). The south-dipping reflector is identified at a depth of about 27 km in the central part of the fault and at a depth of about 34 km in the southern part of the fault, and

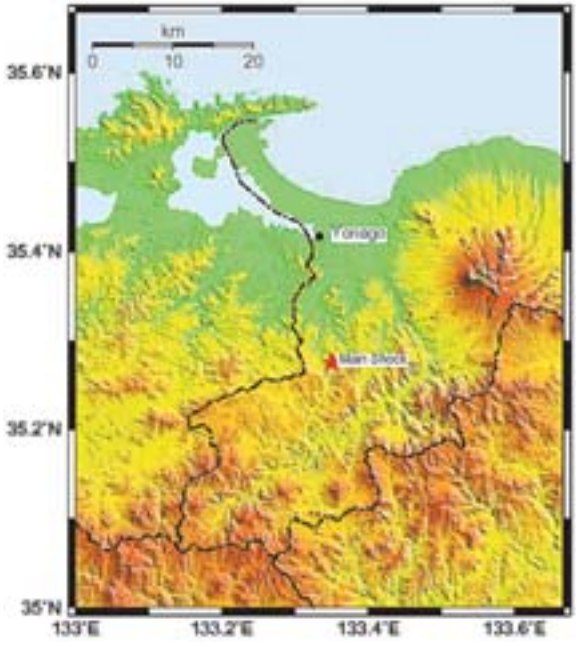

Fig. 1.1 The source area of the 2000 Western Tottori Prefecture earthquake. The red star indicates the main shock.

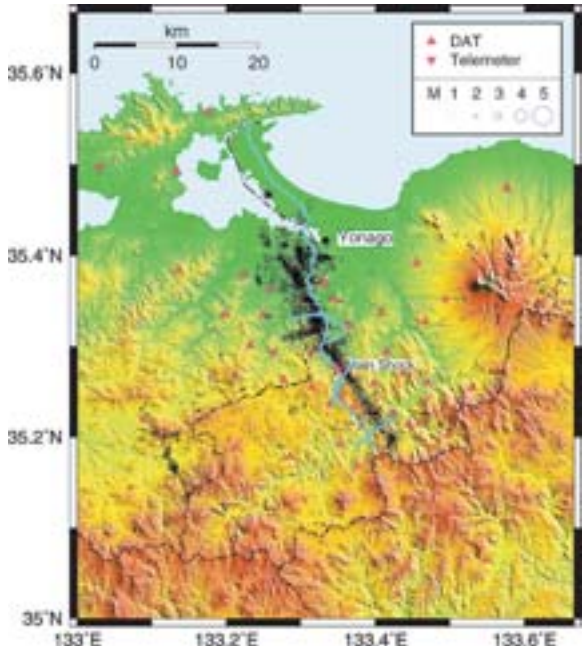

Fig. 1.3 Topographic map of the Western Tottori Prefecture showing the locations of seismic lines (blue lines) and aftershock distribution (circles).

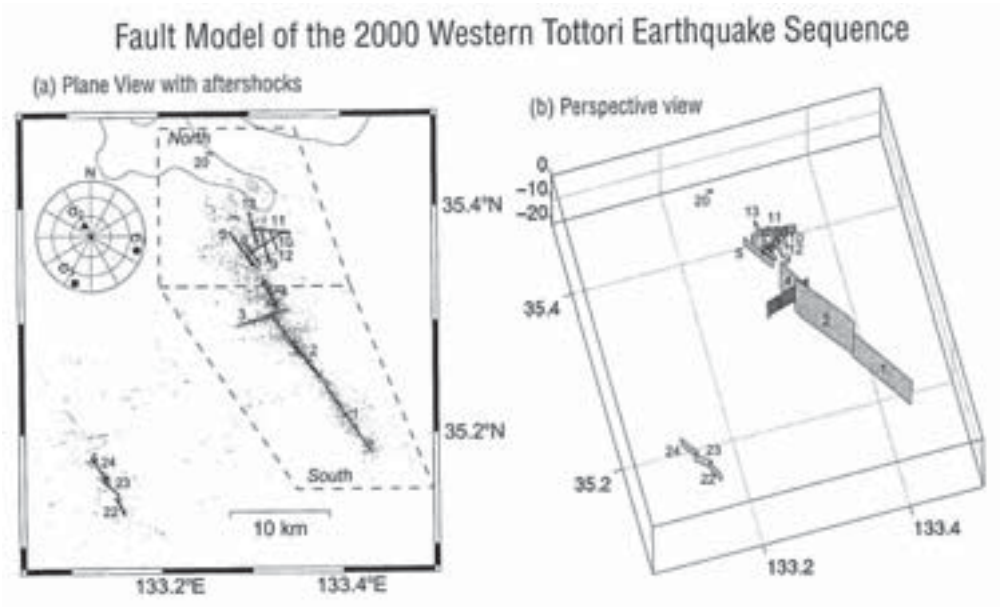

Fig. 1.2 Fault model by Fukuyama *et al*. (2003).

north-dipping reflector was marked from about 45 km at the southern part of the fault to about 55 km at the central part of the fault. Aftershocks were distributed above the reflector (A) in the southern part of the aftershock area. Aftershocks and reflectors were distributed shallower in the northern part than in the southern part. This fact indicated that the distribution of the reflectors corresponded to the aftershock distribution.

1.1.2 Scattering imaging method

Matsumoto *et al*. (2002) conducted the array observation at the central part of the fault area using vibrators, which were the same as Kurashimo *et al*. (2001) used. They estimated a *P* wave scatterer distribution. The area with high strength of scattering was found just below the point of an initial rupture and at a depth of 20 km in the northwestern part of the main shock. The slip distribution of the main shock (Iwata and Sekiguchi, 2002)

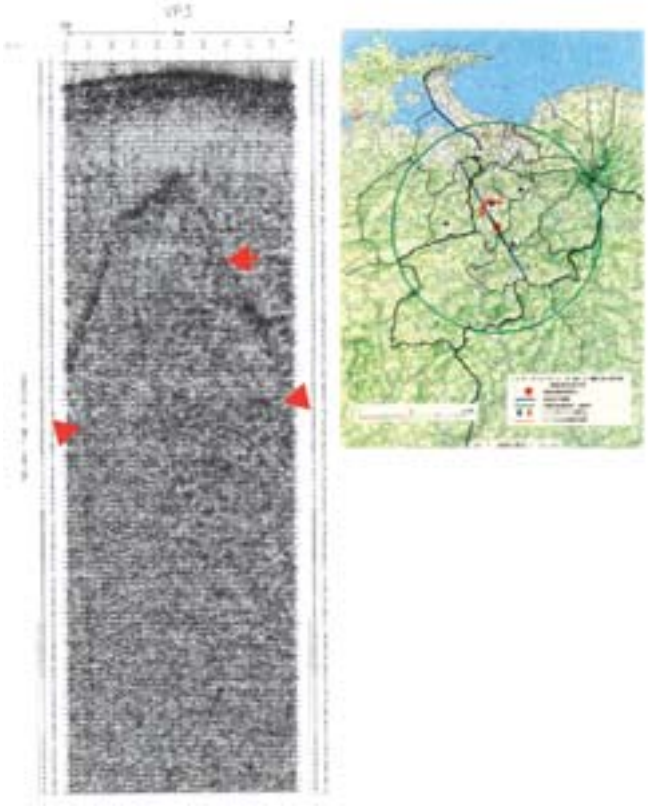

Fig. 1.4 Shot gather of Kurashimo *et al*. (2001). The reflected waves are recognized at two-way travel times of 3.5 and 6 s showing as red arrows.

did not overlap this area with high strength of scattering. They indicated a possibility that the heterogeneity with a wavelength of 100 – 400 m affected the rupture process of the main shock.

Kawamura *et al*. (2003) estimated a *P* wave scatterer distribution. They used four vibrators, which were operated by Kurashimo *et al*. (2001), as a seismic source, and off-line recorders, which were deployed by the Joint Group for Dense Aftershock Observation (2001), as seismic receivers. In the vertical cross-section along the main fault, at depths from the surface to 5 - 7 km, the scatterer strength was high and the aftershock distribution was poor. Moreover, in the vertical cross-section across the main fault, the area with high scatterer strength did not overlap the area of aftershocks.

1.1.3 Seismic tomography

The Joint Group for Dense Aftershock Observation (2001) carried out a dense aftershock observation in and around the source region. They located 1089 aftershocks during the period from 15 to 25 October, 2000, and picked 68177 *P* times and 61922 *S* times. They obtained a travel time tomography image of a 3-D velocity distribution. The high velocity patches were distributed at a depth of 10 km. These high velocity patches did not overlap the rupture area of the main shock.

These observations or experiments detected relationship among reflectors, scatterer, and aftershock distributions, but the resolution of the scatterers or the tomography was about several kilometers. Although Kurashimo *et al*. (2001) and Nishida *et al*. (2002) conducted wide-angle reflection surveys in the source region, the image of the shallow zone was not good enough to be resolved. Since the reflection line of Abe *et al*. (2001) almost crossed the main fault, the crustal image along the fault was not analyzed.

Since the reason why a surface rupture was not clearly observed is considered to be the effect of the fine-scale heterogeneity in the shallow part of the crust, it is needed to image more fine crustal structure.

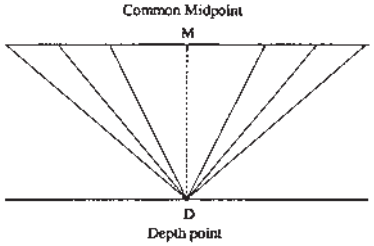

Fig. 1.5 Common midpoint ray paths under three fold coverage (Scales, 1995).

1.2 A new method for imaging the crust

A common midpoint (CMP) reflection method is widely used to image the heterogeneous crustal structure. A resolution of the CMP method is higher than that of other methods, including a common scatterer point (CSP) method and a seismic tomography method.

Sources and receivers used in the CMP method are located on or near the surface. The sources, such as explosions or vibrators, are controlled in their locations and origin times. The receivers are deployed in arrays. The fold of a CMP gather is the number of source and receiver pairs for each midpoint. This is illustrated in **Fig. 1.5** (e.g. Scales, 1995), which shows three-fold coverage. The CMP gathers are transformed into a zero-offset reflection record by normal move-out (NMO) corrections. The NMO corrected traces are stacked to improve signal-to-noise ratios. The stacked zero-offset record is usually called a stacked time section. The seismic reflection method to obtain the stacked section from the multi-fold CMP records is referred to as the CMP reflection method.

The CMP method assumes that the reflectors are horizontally layering. However, the assumption of purely horizontal layering is not the case but layers sometimes dip in the stacked section. Therefore, a post-stack migration is applied to the stacked section to transform the apparent dip in the zero-offset seismic sections into a true dip.

In contrast, a vertical seismic profiling (VSP) method consists of recording the waveform at regularly and closely spaced depth

receivers. The most common VSP in vertical holes, a zero-offset VSP, uses a single source located near a wellhead. In an offset VSP, the source is located at some distance from the borehole. In a reverse VSP, the sources are located in the borehole and the receivers are located on the surface.

Both the CMP method and the VSP method use a controlled source. The advantage of the controlled source is that the location and the shot time are known. The limitation of the controlled source, however, is the magnitude and the number of sources practically used in an exploration. The dynamite can provide a large magnitude source, but amount of chemical charge size is limited due to safety reasons. On the other hand, the vibrator can provide dense source locations, but the energy of its single shot is very weak. The vibrator method is innovated to improve the signal-to-noise ratio by using a controlled waveform source.

Since the sources of the controlled seismology are generally located on the surface, the distance between the aimed reflector and the source is long. The source generating *P* wave is easy to be developed, but *S* wave source is difficult especially for a large energy source. If the natural earthquakes at depth in the crust are used as the sources in the seismic reflection profiling method, it may improve crustal images as compared to the conventional method. The advantages of using natural earthquakes are (1) the distance between the source and the reflector can be short, (2) the energy of the source is larger than that of the controlled source, and (3) *S* wave energy is easy to be used. The disadvantage are (1) the occurrence of earthquakes in the survey area is unknown, (2) the origin time and location of earthquake are unknown to be estimated with inherent errors, and (3) the radiation pattern is also unknown to be estimated from observed data.

In this study, I developed a new method to image the reflectors using natural earthquakes, and applied the aftershocks of the 2000 Western Tottori prefecture earthquake. Since I used aftershocks as the sources of new method, the first disadvantage is resolved. So, I tried the other two problems by the very accurate observations and stacking the widely distributed earthquakes, which are discussed in the following sections.

2. Method

2.1 Introduction

Seismic sources and receivers in a conventional reflection profiling method are located on or very near the surface. The conventional processing method of surface seismic reflection data incorporates common midpoint (CMP) stacking with normal move-out (NMO) corrections.

Since the natural earthquakes are not located on the surface of the earth, I cannot use the usual CMP method. Therefore, I propose a new method, the Natural Earthquake Reflection Profiling (NERP) method, to image the crust using natural earthquakes. In this chapter, the NERP method is introduced.

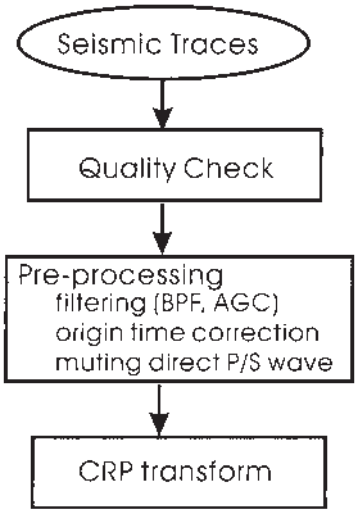

Fig. 2.1 Flow chart of the NERP method.

2.2 NERP method

The main flow of the NERP method is shown in **Fig. 2.1**. The NERP method consists of three steps, (1) quality check of seismic traces, (2) pre-processing, and (3) common reflection point (CRP) transform and re-sampling.

2.2.1 Quality check of seismic traces

In general, the measurements made in geophysical exploration are contaminated by unavoidable noises. These noises are divided into two categories, a natural noise and an artificial noise. Commonly, the most prevalent methods to increase the signal-to-noise ratio of seismic records are (1) to increase the power of the source, (2) to average out the noise by increasing the number of shots, and (3) to move receivers to less noisy locations, if available. In controlled seismic experiments, since the noises were monitored in seismic records by an on-line recording system, the records were edited out in real time.

On the other hand, since the origin time and location of the natural earthquake are unknown in real time, the noises were recorded with earthquakes. To exclude the noise events, all seismic records were processed after the observation. I inspected all the data by eyes and edited them manually.

2.2.2 Pre-processing

The pre-processing consisted of three parts, (1) filtering, (2) time correction, and (3) muting. On step (1), the seismic data was band-pass filtered and the automatic gain control was applied to them. On step (2), the correction of the origin time was applied to each seismic trace. On step (3), the direct P- and S- waves were muted.

2.2.3 CRP transform and re-sampling

Since the NERP method uses the natural earthquakes, the seismic sources are not located on the surface of the earth. Therefore, the reflection point does not remain at a mid-point of the source and the receiver as the distance between the source

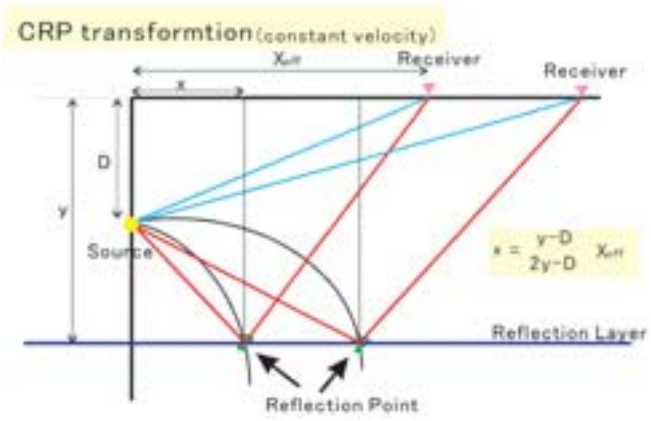

Fig. 2.2 Schematic illustration showing the CRP transformation.

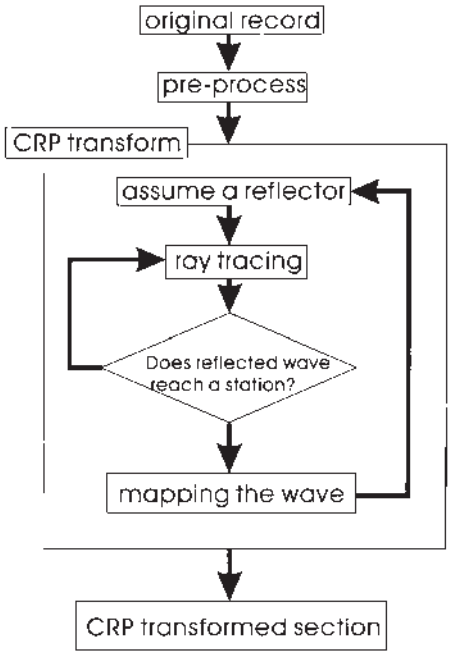

Fig. 2.3 Flow chart of the CRP transformation.

and the reflector increases. The concept of the CMP method is not useful in this source-receiver geometry and another data processing method is needed.

I incorporate a common reflection point (CRP) transformation, which is similar to that used in the reverse offset vertical seismic profiling (VSP) method (Dillon and Thomson, 1984). **Fig. 2.2** outlines the principle of the mapping technique for a horizontal reflector in a constant velocity situation. The formula transforms a time (t) on a seismic trace at a distance (x) to a distance (x) - depth (y) domain of the CRP point in the subsurface.

A distance x between a CRP point and a source in a constant velocity medium is given by $x=(y-D/2y-D)X_{\mathrm{off}}$, where X_{off} is a distance between the source and the receiver, D is a depth of a source, and y is a depth of an assumed reflector. Note that if the source is located on the surface, then D is zero and x is simply half of X_{off}. Also, if the reflector is deep enough to be $y << D$, then x is also a half of X_{off}. That is, the CRP transform includes the CMP method as a limited case.

For real data with a complex velocity structure, ray-tracing techniques must be used for calculating CRP points. **Fig. 2.3** shows the flow of the CRP transformation. The CRP transformation consists of following five steps. (1) I assume a reflector at a depth of the event. (2) I calculate CRP points and travel times between all the combinations of the source and the receivers. In this study, I used the *TRAVEL* subroutine, which is one component of *HYPOMH* (Hirata and Matsu'ura, 1987), to calculate travel times and CRP points. (3) I map the amplitude of the waveform equivalent to the calculated travel time onto the CRP point. (4) I assume the reflector at the next depth Δd deeper, and repeat the procedure of (2)-(4). (5) I get the CRP transformed image of the single event. **Fig. 2.4** shows an example of the record section, and **Fig. 2.5** shows the CRP transformed section. The vertical resolution of the CRP transform is prescribed by the vertical discretization length, Δd, which should be less than the minimum wave length of recorded signals contained in the seismic records, which is discussed in the following. The CRP transform relocates the data (and re-samples to a regular grid) to place the reflectors at the points assuming that reflectors are horizontally located, which is also assumed in the conventional NMO correction.

The horizontal resolution is measured in terms of Fresnel zone, $H=\sqrt{h\lambda/2}$, where h is a target depth, and λ is a wavelength. This is the same as that used in usual reflection seismology. Exactly, the target depth is determined by both depths of the source and reflector. In general, as the NERP uses the sources at depth, h can be smaller than that assumed in a conventional reflector depth from surface. The earthquakes, however, distributed at different depths and I simply assumed h as a depth of reflector. A typical horizontal resolution in the present study ranges from 150 to 1300 m at depths from 1 to 30 km assuming wave lengths of 60 m to 120 m.

The vertical resolution is governed by a wavelength of the probing wave: $\lambda/4$. Therefore, the vertical resolution of a 50-Hz seismic wave propagating in a medium with a wave speed of 3 km/s, which corresponds to a wave length of 60 m, is about 15 m. According to the vertical resolution, I use 10 m as Δd.

In the NERP method, we have to assume a mode of traveling wave either as *P* or *S* wave for incident and reflected waves: *PP*, *PS*, *SP*, *SS*. In the following session, I propose a method to resolve these modes in real data.

2.3 Numerical experiment

I assumed a 4-km-long seismic array with a receiver spacing of 50 m. A seismic source was assumed to be located at a depth of 5 km and a horizontal distance of 3 km from the end of the seismic array. Three-layered velocity structure shown in

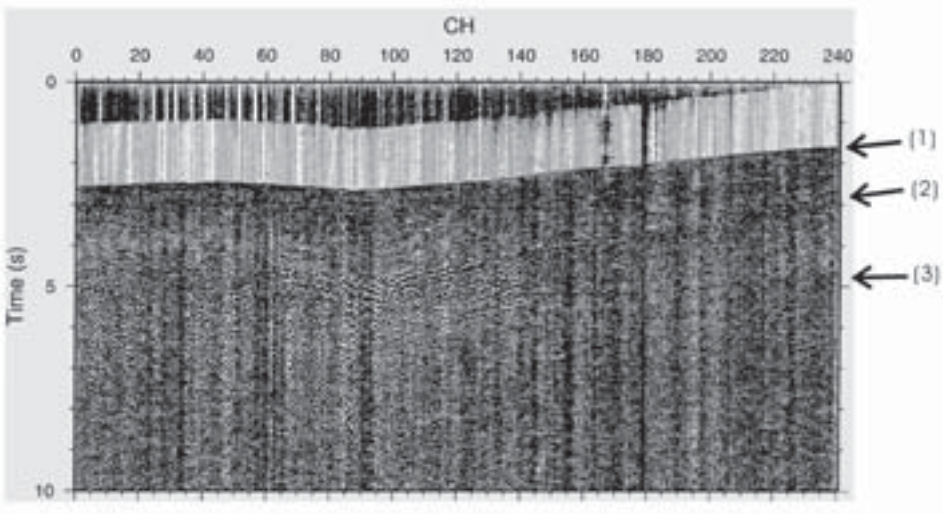

Fig. 2.4 The example of record section. (1) indicates the direct *P* wave, (2) indicates the direct *S* wave, and (3) indicates the reflection.

Table 2.1 Three layered velocity model for numerical experiment.

Depth (km)	Vp (km/s)
0	
	5.88
3	
	6.04
11	

Table 2.1 was assumed. I assumed a single reflector at a depth of 11 km. These settings are shown in **Fig. 2.6**. I calculated the synthetic seismograms including direct *P* and *S* waves, and *PP*, *SP*, *PS*, and *SS* reflected waves, which appear four separate phases. A common shot gather record of the synthetic data is shown in **Fig. 2.7**.

I applied the NERP method to the synthetic data assuming *PP*, *SS*, *SP*, or *PS* reflections (**Fig. 2.8**). If I assume the signal is *PP* reflection, the reflected *PP* wave appears horizontally at a depth of 11 km, although the other phases *SP*, *PS*, and *SS* appear with a dip and curvature below the *PP* waves.

If I assume that all the signals are *SS* mode, only the *SS* signal is imaged at a depth of 11 km, and the other waves appear with a dip and curvature. Also, for *PS* and *SP* mode, signals that correspond to the real mode appear at a real depth without fictitious dips and curvatures.

Therefore, I propose to resolve different mode of the seismic reflection wave as follows: we transform the data under the assumption with *PP*, *PS*, *SP*, or *SS*. The images that commonly appear in the different assumption are judged as real reflectors.

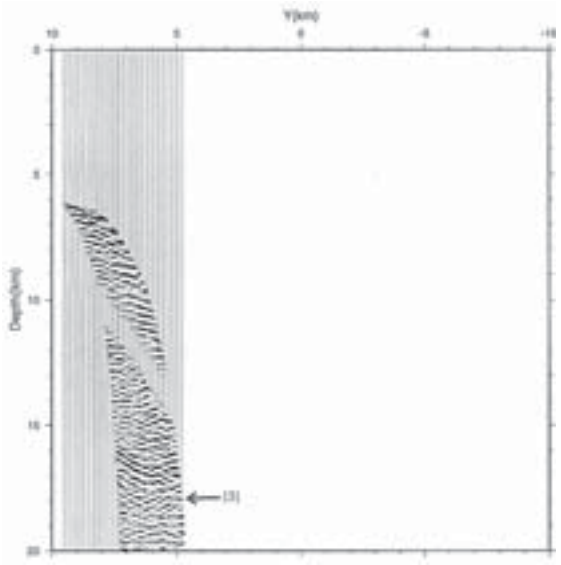

Fig. 2.5 The CRP transform of the seismic records in **Fig. 2.4**. Note that the first arrival phases of P- and S-waves, which are indicated by arrowheads with labels (1) and (2) in **Fig. 2.4**, are muted out. The later phase indicated with a label (3) is shown, which corresponds to that shown in **Fig. 2.4** by the arrowhead with a label (3).

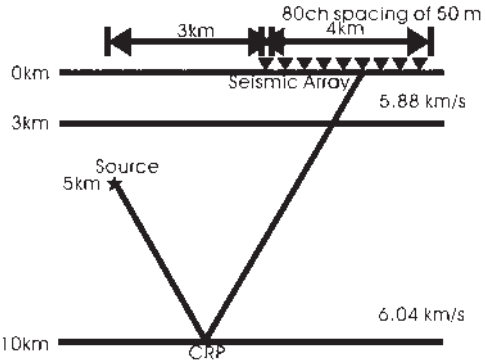

Fig. 2.6 Schematic illustration showing the setting of the numerical test.

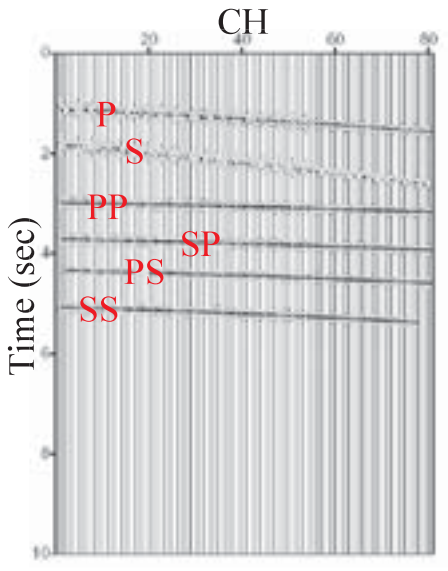

Fig. 2.7 Synthetic seismogram of numerical experiment.

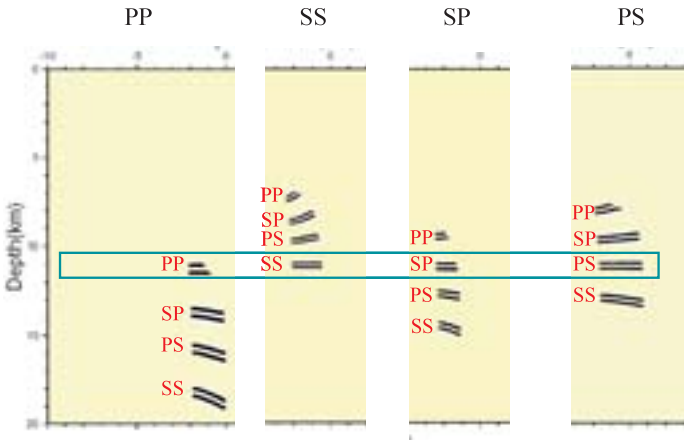

Fig. 2.8 The result of numerical experiment.

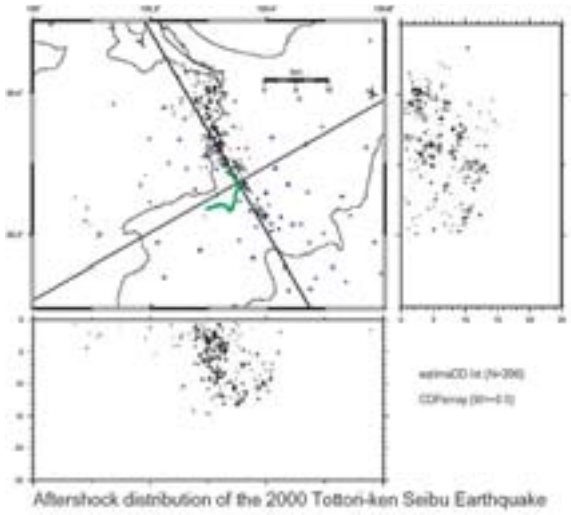

Fig. 3.1 Map showing the multi-channel seismic array (green line), the seismic stations of very dense aftershock observation (blue crosses), and the aftershock distribution (circles).

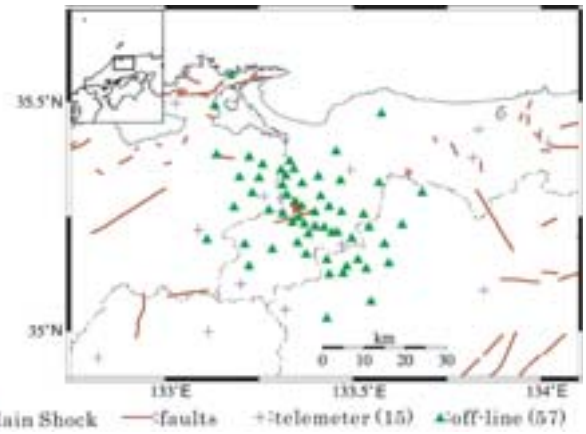

Fig. 3.2 Map showing the seismic stations of the Joint Dense Aftershock Observation.

3. Observation and data

3.1 Introduction

The aftershock observations and the reflection surveys were conducted in the source region of the 2000 western Tottori Prefecture earthquake. In this study, I used the aftershocks to image the crustal structure. I participated in two aftershock observations, a multi-channel aftershock observation and a very dense aftershock observation.

3.2 Multi-channel Aftershock Observation

A multi-channel aftershock observation was conducted to reveal the heterogeneous crustal structure in the fault area of this earthquake. A multi-channel seismic array was deployed along and across the main fault area. A length of the multi-channel seismic array is 12 km. Each channel was equipped with nine vertical-component seismometers with a natural frequency of 10 Hz. The array consisted of 240 channels with a receiver spacing of 50 m. The signal was recorded with the GDAPS-4 digital telemetry system (Iwaki *et al*., 1991) at a sampling rate of 4-ms. The multi-channel array was operated for 85 hours from 17:00 on October 21 (JST) to obtain quasi-continuous records of aftershocks. Two hundred and ninety-six events were recorded in the multi-channel array. **Fig. 3.1** shows the location of the multi-channel seismic array.

3.3 Very Dense Aftershock Observation

The Joint Group for Dense Aftershock Observation carried out a dense aftershock observation in and around the source region. Fifty-seven temporary offline stations were deployed. All the temporary stations were equipped with a 3-component

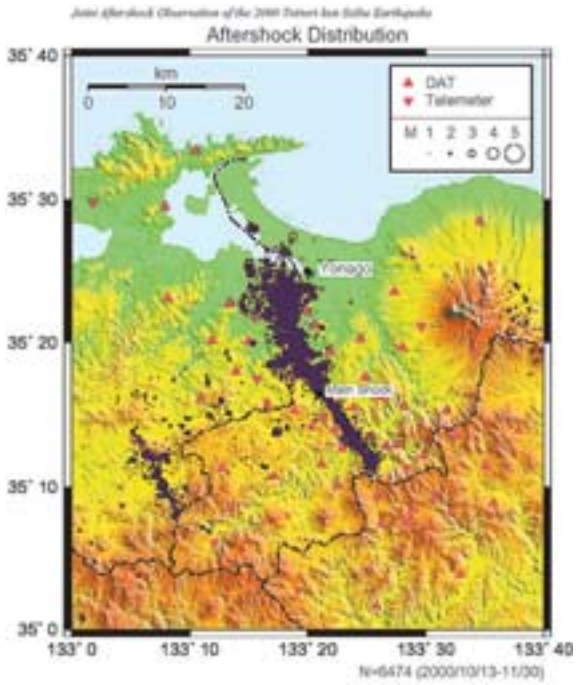

Fig. 3.3 Map showing the aftershock distribution (blue circles).

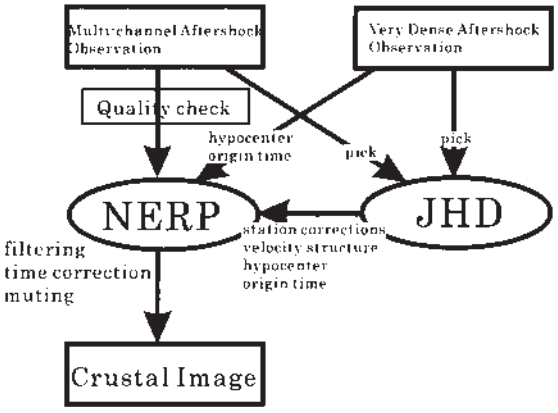

Fig. 4.1 Flow chart of data processing.

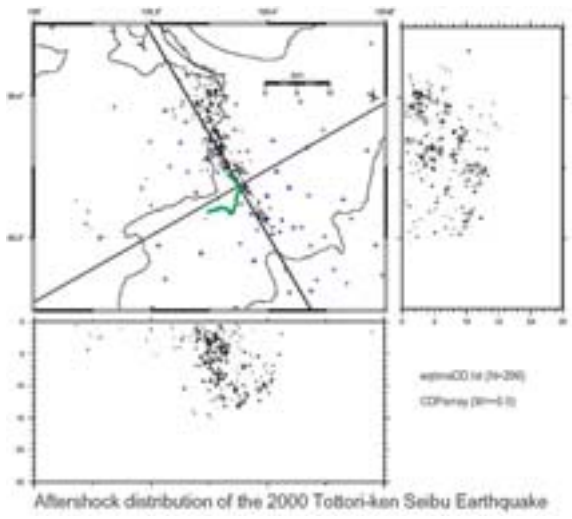

Fig. 4.2 Map showing the aftershock distribution as black circles recorded by the multi-channel seismic array observation.

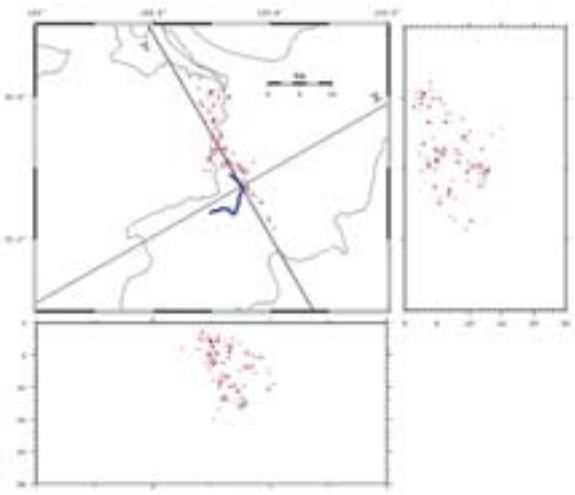

Fig. 4.3 Map showing the hypocenters of selected earthquakes (red circles).

seismometer with a natural frequency of 0.05, 1.0, 2.0, or 4.5 Hz. Their waveform data were merged with those from 15 permanent telemeter stations in the same region. **Fig. 3.2** shows the distribution of the temporary and permanent seismic stations. The observation started on 13 October and continued for one and half month.

During this period, there are about 7,000 events in the JMA unified earthquake list. All data of temporary stations were edited into event data by the JMA unified earthquake list. The format of edited data is the *win*-format (Urabe, 1994). Then I processed the temporary and telemeter data to analyze.

Chiba *et al*. (2003) picked *P* and *S* wave arrivals of the combined data using a new algorithm for automatic phase picking, and relocated hypocenters using the double-difference earthquake location algorithm (Waldhauser and Ellsworth, 2000). The hypocenter distribution is shown in **Fig. 3.3**.

4. Analysis and Result

4.1 Introduction

The NERP method strongly relies on the origin time and hypocenter of earthquakes, and the background velocity structure. The main flow of the analysis is shown in **Fig. 4.1**. To obtain accurate estimates of origin times and hypocenters

Table 4.1 The initial velocity model for JHD.

Depth (km)	Vp (km/s)
0	
	5.88
3	
	6.04
16	
	6.60
32	
	8.00

Table 4.2 The final velocity model calculated by JHD.

Depth (km)	Vp (km/s)
0	
	5.76
3	
	5.94
16	
	6.60
32	
	8.00

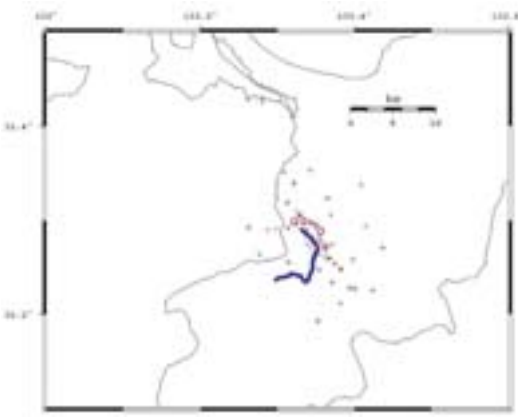

Fig. 4.4 Map showing the distribution of epicenters (red circles) and seismic stations (blue line and crosses) for the JHD method.

of the earthquakes good enough for reflection imaging, I used the travel-time data by the Joint Group for Dense Aftershock Observations (2001) together with the multi-channel array data. As the pre-processing of the NERP method, I relocate earthquakes using the joint hypocenter determination method.

4.2 Quality check of data

Two hundred and ninety-six seismic events are recorded by the multi-channel aftershock observations (**Fig. 4.2**). To exclude noisy events, I carefully checked all the trace of recorded events (about 70,000 traces). I selected 81 events among them as good for analyzing. **Fig. 4.3** shows the hypocenter distribution of 81 events. Then, I picked the *P* wave arrivals of each trace and marked noise traces.

4.3 Very accurate earthquake relocation

To estimate the accurate origin time and hypocenter, the Joint Hypocenter Determination (JHD) method (Kissling *et al*., 1994) is applied. The JHD method simultaneously estimates earthquake locations, origin times, a 1-D (layered) velocity structure, and station corrections.

I used an initial 1-D velocity structure with four layers, as shown in **Table 4.1**. The velocity structure used for initials was determined by Chiba *et al*. (2003) using the very dense aftershock observation data. The *S* wave velocity is assumed to be $1/\sqrt{3}$ of the *P* wave speed.

In the first step, I selected 31 events located in and around the array. Since the array was equipped with only vertical components, 24 temporary seismic stations with 3-component seismograph around the array were also used. **Fig. 4.4** shows the distribution of used epicenters and seismic stations.

Fig. 4.5 shows comparison of travel time residuals of the initial hypocenter located by the velocity structure previously estimated and those by the relocated hypocenter with re-determined velocity structure and station corrections of the array channels. The root-mean-square (RMS) of *P* wave travel time residuals is reduced from 170 ms to 14 ms.

The estimated station corrections are shown in **Fig. 4.6**, which are correlated with an altitude of each station (**Fig. 4.7**). The station corrections and the station altitudes have a positive correlation. Although the altitudes are taken into account for location algorithm, the result represents that there still exists a small difference between a modeled velocity and the real one, and heterogeneity in the upper most crust near the receiver is well modeled by the station corrections. The final 1-D velocity model is shown in **Table 4.2**.

In the second step, the origin times and depths of the other 50 earthquake were re-determined by the JHD method with the station corrections and the 1-D velocity structure determined in the first step. Since these 50 earthquakes were apart from the array, I fixed the epicenters of the events determined by the very dense aftershock observation data (Chiba *et al*., 2003). The RMS of *P* wave travel time residuals is reduced from 180 ms to 24 ms (**Fig. 4.8**).

4.4 Apply the NERP method

Before applying the NERP method, the seismic data was pre-processed. The pre-processing onsisted of three steps, (1) filtering, (2) time correction, and (3) muting. In step (1), the automatic gain control (AGC) with a time window of 4 s was applied to the data, and the data was filtered with a pass-band from 10 to 20 Hz. In step (2), a correction of the origin time between the catalog and the calculation using the JHD method is applied to each seismic trace. The hypocenters or depths of the earthquakes are also corrected according to the previous results. In step (3), the direct *P* wave and *S* wave are muted, and the noisy traces are removed from the data set. The mute length is 1.0 s with both ends of a cosine taper of 0.3 s.

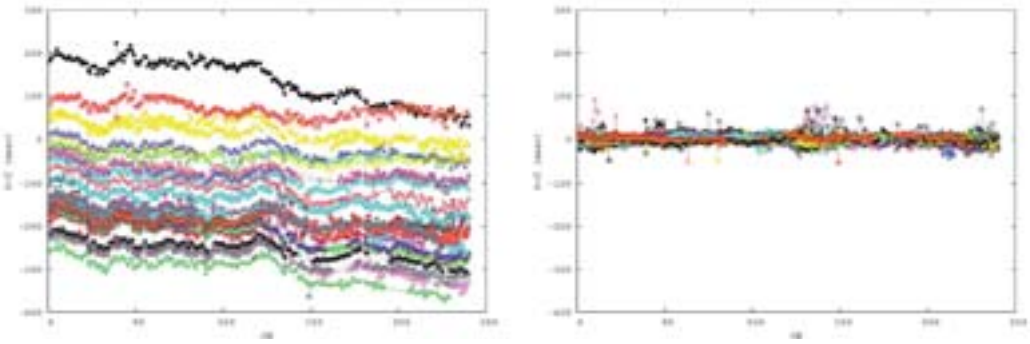

Fig. 4.5 The initial (left) and result (right) of travel time residuals.

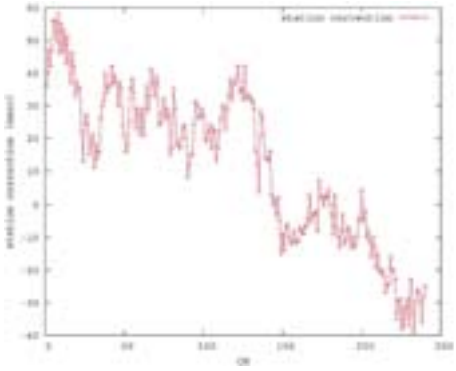

Fig. 4.6 Station corrections.

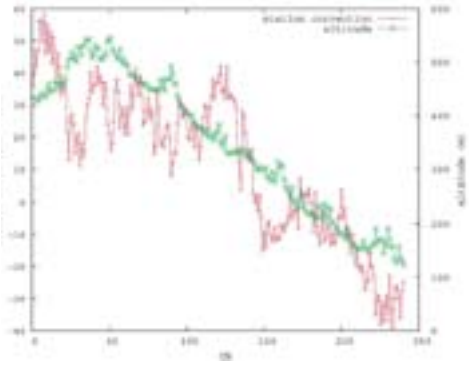

Fig. 4.7 Comparison between the station corrections and the altitude of each station.

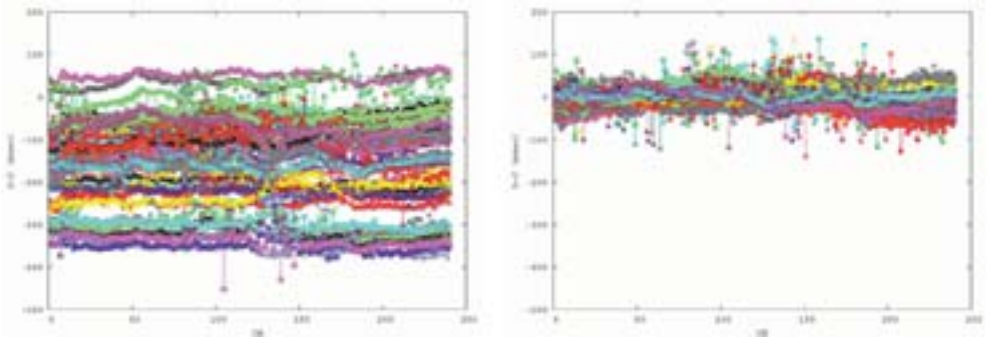

Fig. 4.8 The initial (left) and result (right) of travel time residuals.

I applied the CRP transformation to the pre-processed data by assuming the *PP*, *SS*, *PS*, and *SP* reflections. I used discrete space coordinate points in a distance-depth domain for re-sampling with a horizontal spacing of 50 m and a vertical spacing of 10 m. Then, I stacked the CRP transformed sections of all events with a horizontal smoothing of 150 m and a vertical AGC length of 15 km. Finally, I obtained the NERP reflection profiles as a stacked distance-depth section.

Because a trajectory of the CRP transformation lies three-dimensionally, I binned traces that are located in the same rectangle, which is define as a bin with the same distance range along the profile but different distance range perpendicular to the profile: in the present study earthquakes are distributed basically in a direction of northwest to southeast, which I denote as a y-axis, and I define a x-axis perpendicular to the y-axis (**Fig. 4.2**). I stacked traces that lie in the same bin. I process the data along the y-axis to make a y-depth cross section with stacking all data of the same y-bin with a width of 50 m along the x-axis.

In case of the x-depth section, as the earthquake distributed widely perpendicular to the profile, I limited earthquakes in the y-direction, which will be described in the later session.

In a *PS* reflection profile, due to the computing problem of calculating the travel times, I did not assume the reflectors between depths of the event and 3 km below the event.

4.5 Result

The final NERP reflection profiles along the main fault, y-direction, with assumptions of *PP*, *SS*, *PS*, and *SP* reflections are shown in **Figs. 4.9 - 4.12**. In all profiles, between depths of 3 and 8 km, several reflectors are visible. Between depths of about 14 and 20 km, several reflectors are shown, suggesting the reflective lower crust.

Since *PP*, *SS*, *PS*, and *SP* profiles image the reflectors at the same depths, especially 7.5 km and 13 km, I can interpret that the reflectors are not the ghost reflection images but the real reflectors.

Figs. 4.13 - 4.41 show the final NERP reflection profiles across the main fault, x-direction, with the assumption of a *PP* reflection. Ranges stacking along y-direction are shown in the figures. All figures have the same characteristics as **Figs. 4.9 - 4.12**.

In the southern part of the main fault (**Figs. 4.13 - 4.16**), no images are found above a depth of 10 km because of no aftershocks. In the other part of the main fault (**Figs. 4.17 - 4.41**), the following common characteristics are recognized. Above a depth of 5 km, image is poor because of few aftershocks. Between depths of 5 and 9 km, several reflectors are visible. Between depths of 9 and 14 km, the reflectors are not clearly found. Below a depth of 14 km, many reflectors are visible.

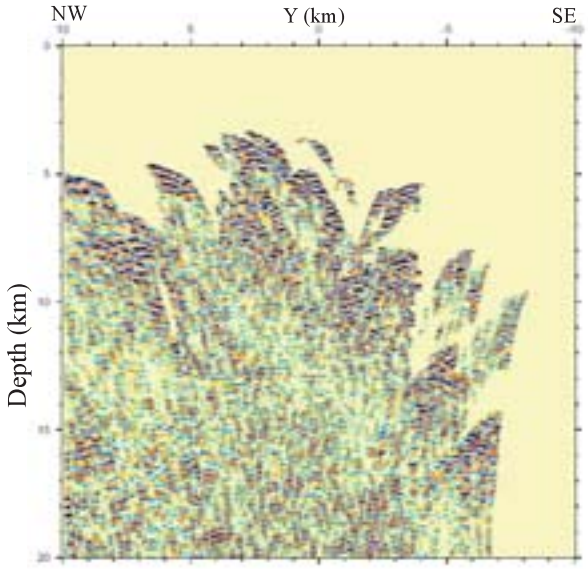

Fig. 4.9 NERP reflection profile assuming *PP* reflection.

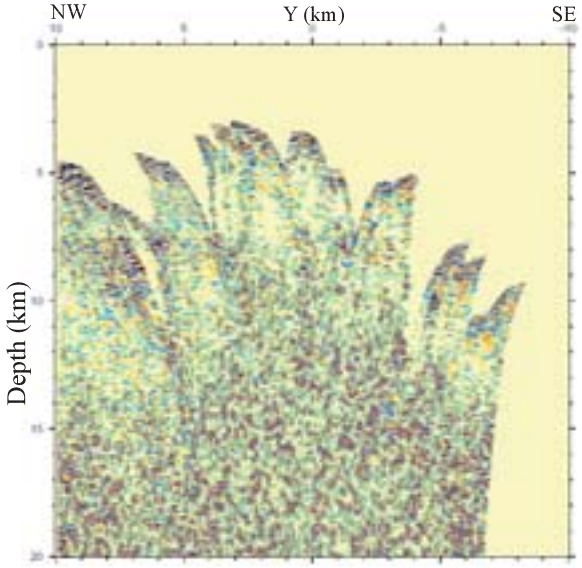

Fig. 4.10 NERP reflection profile assuming *SS* reflection.

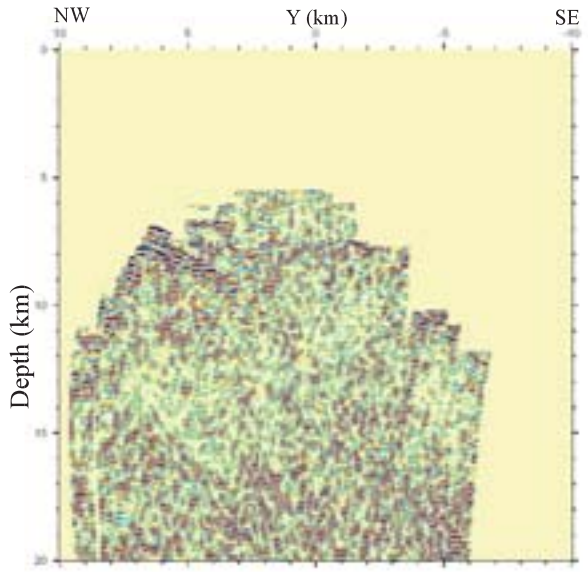

Fig. 4.11 NERP reflection profile assuming *PS* reflection.

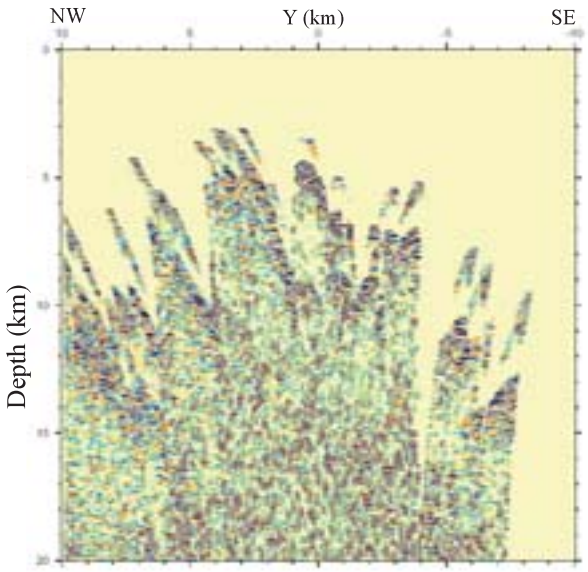

Fig. 4.12 NERP reflection profile assuming *SP* reflection.

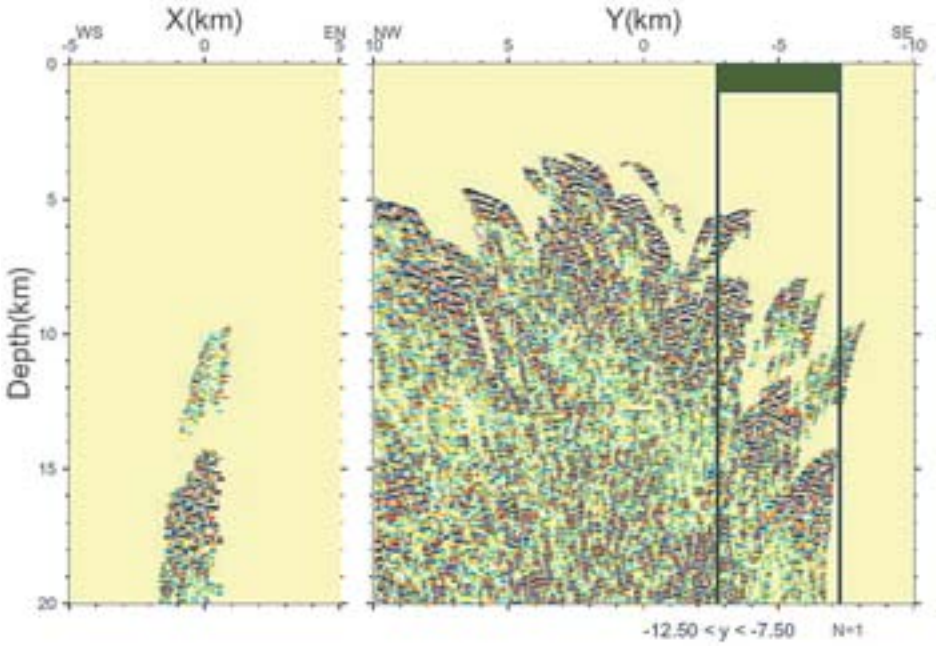

Fig. 4.13 NERP reflection profile along (Y) and across (X) the fault. Green rectangle indicates the range stacking along y-direction.

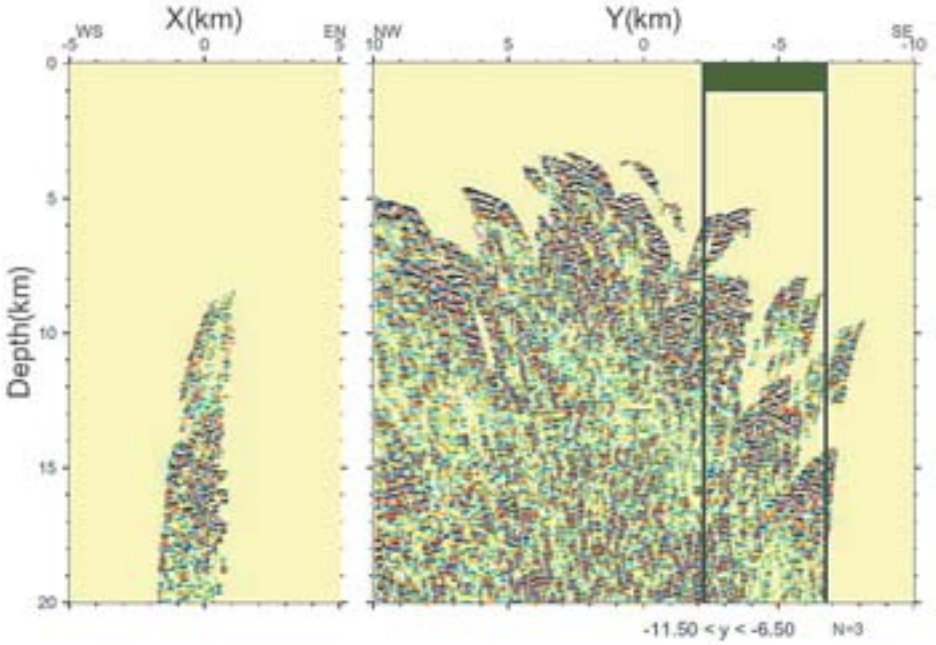

Fig. 4.14 NERP reflection profile along (Y) and across (X) the fault.

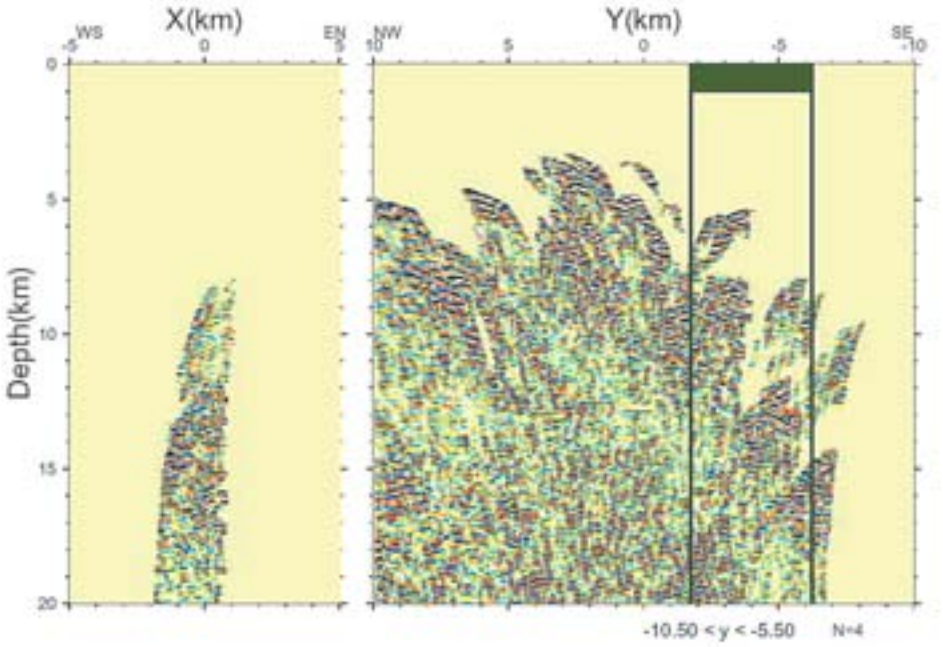

Fig. 4.15 NERP reflection profile along (Y) and across (X) the fault.

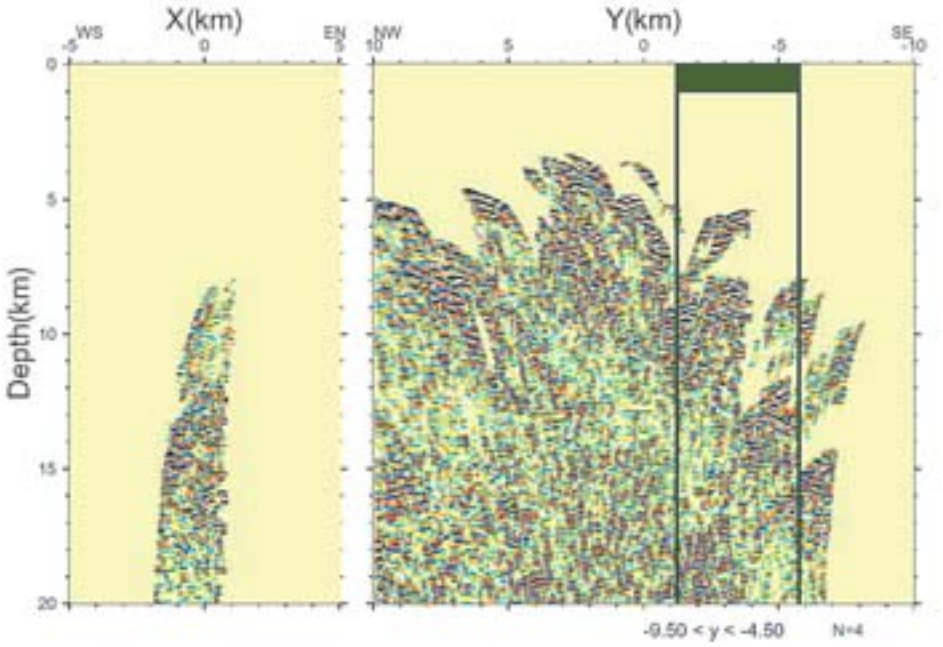

Fig. 4.16 NERP reflection profile along (Y) and across (X) the fault.

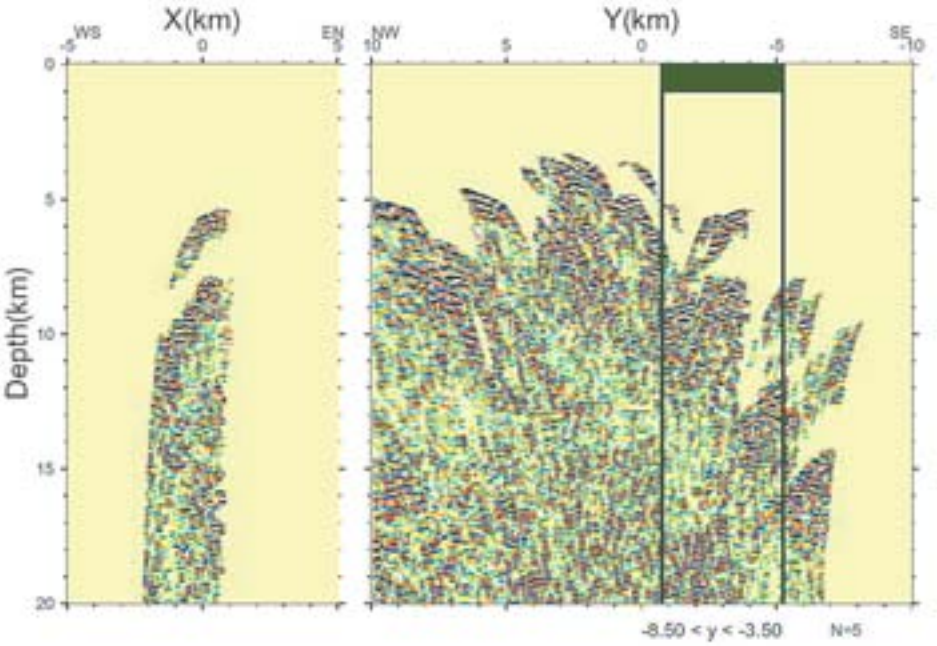

Fig. 4.17 NERP reflection profile along (Y) and across (X) the fault.

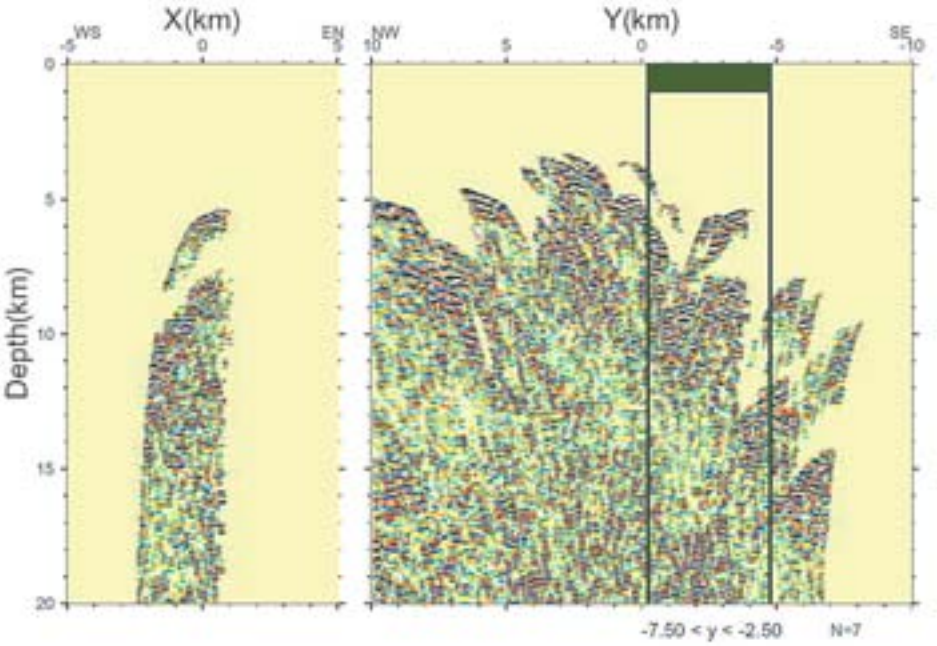

Fig. 4.18 NERP reflection profile along (Y) and across (X) the fault.

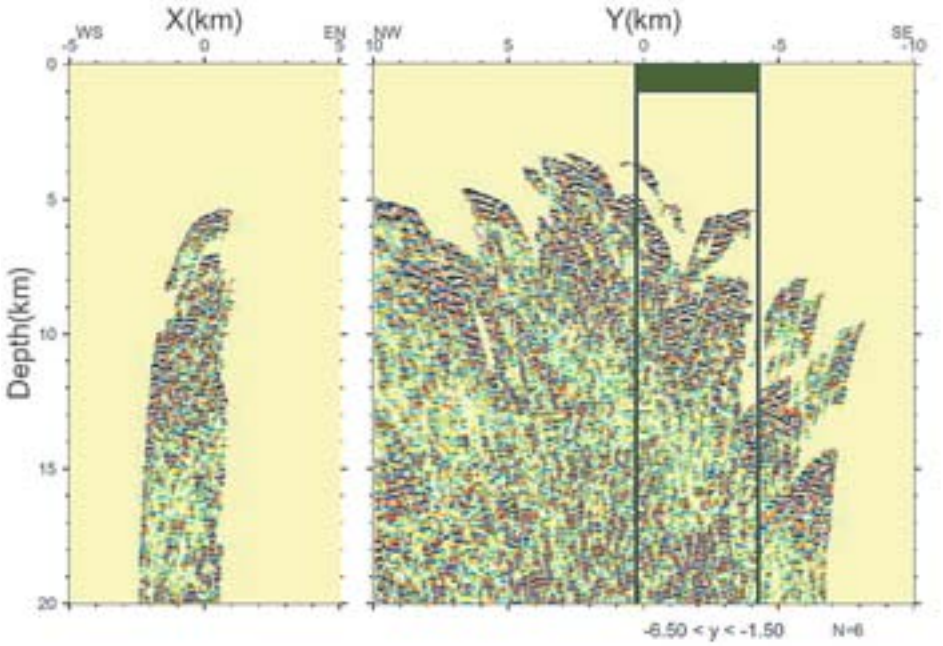

Fig. 4.19 NERP reflection profile along (Y) and across (X) the fault.

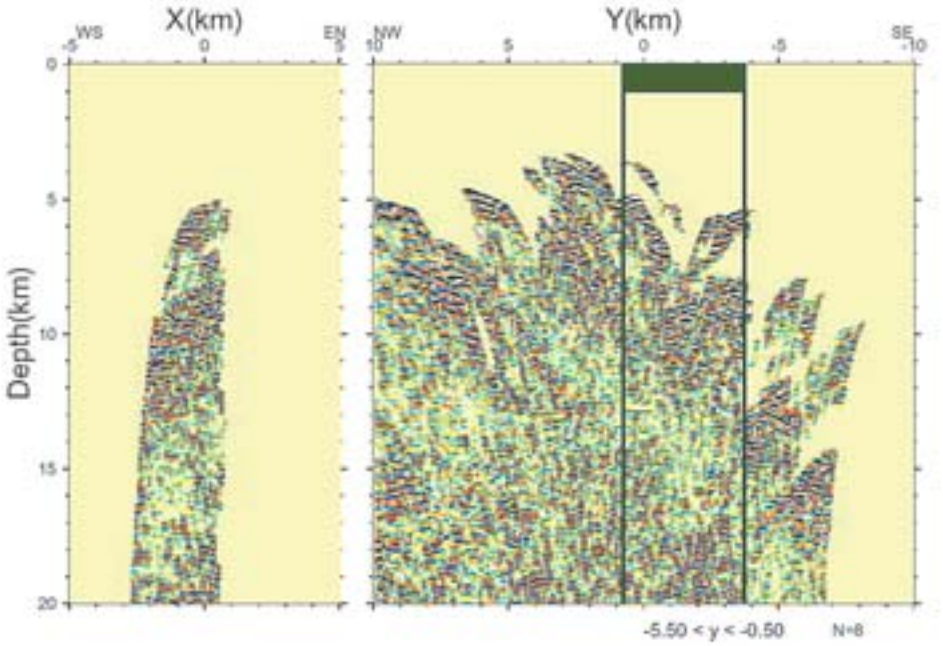

Fig. 4.20 NERP reflection profile along (Y) and across (X) the fault.

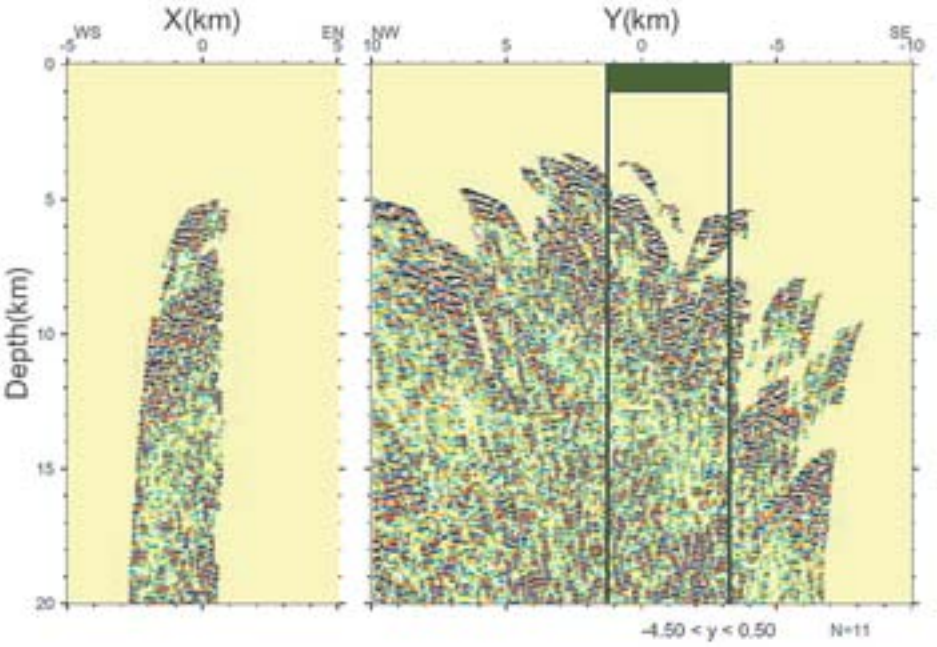

Fig. 4.21 NERP reflection profile along (Y) and across (X) the fault.

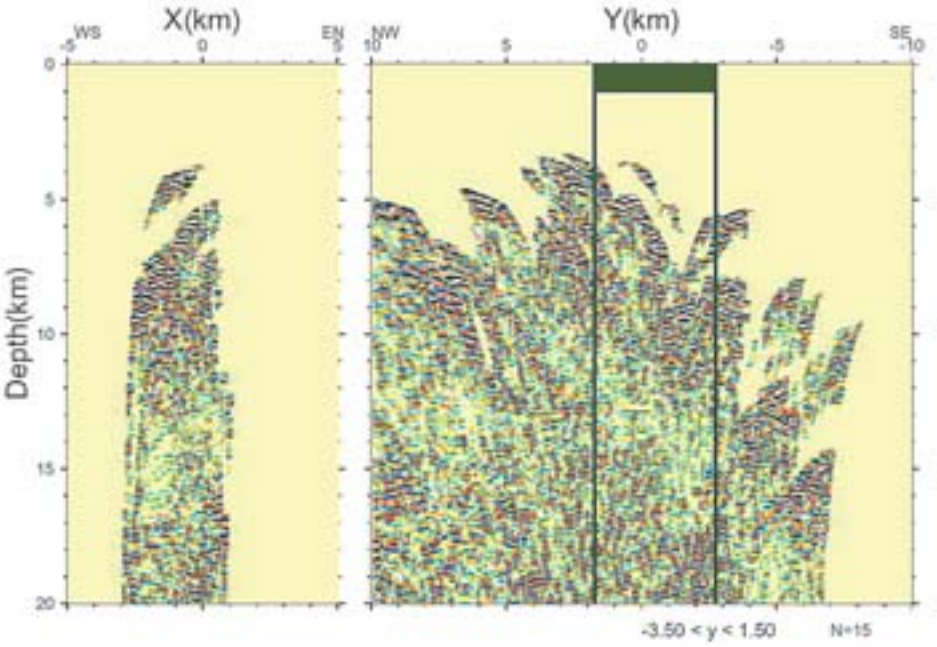

Fig. 4.22 NERP reflection profile along (Y) and across (X) the fault.

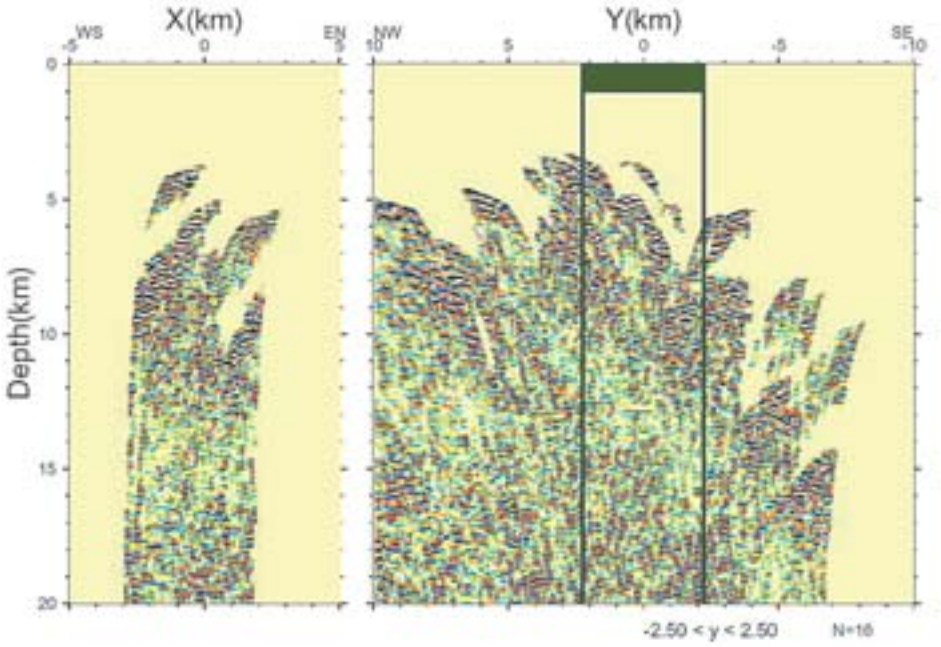

Fig. 4.23 NERP reflection profile along (Y) and across (X) the fault.

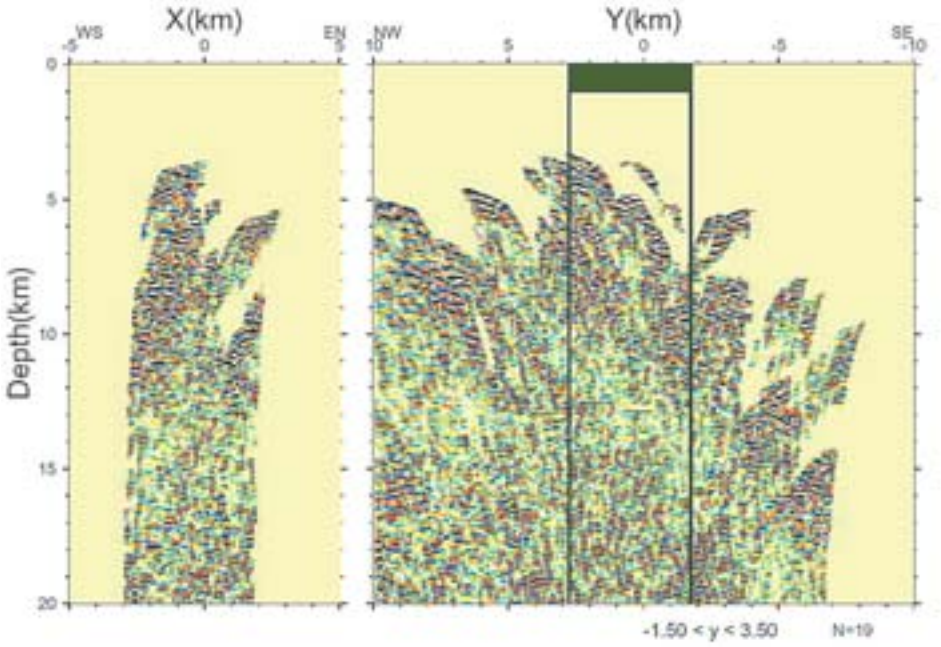

Fig. 4.24 NERP reflection profile along (Y) and across (X) the fault.

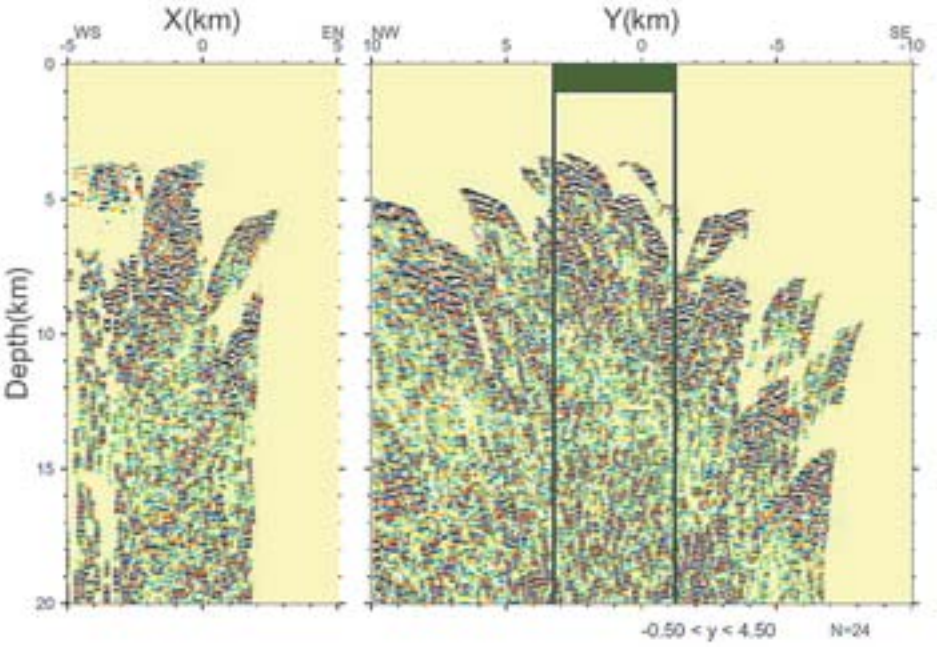

Fig. 4.25 NERP reflection profile along (Y) and across (X) the fault.

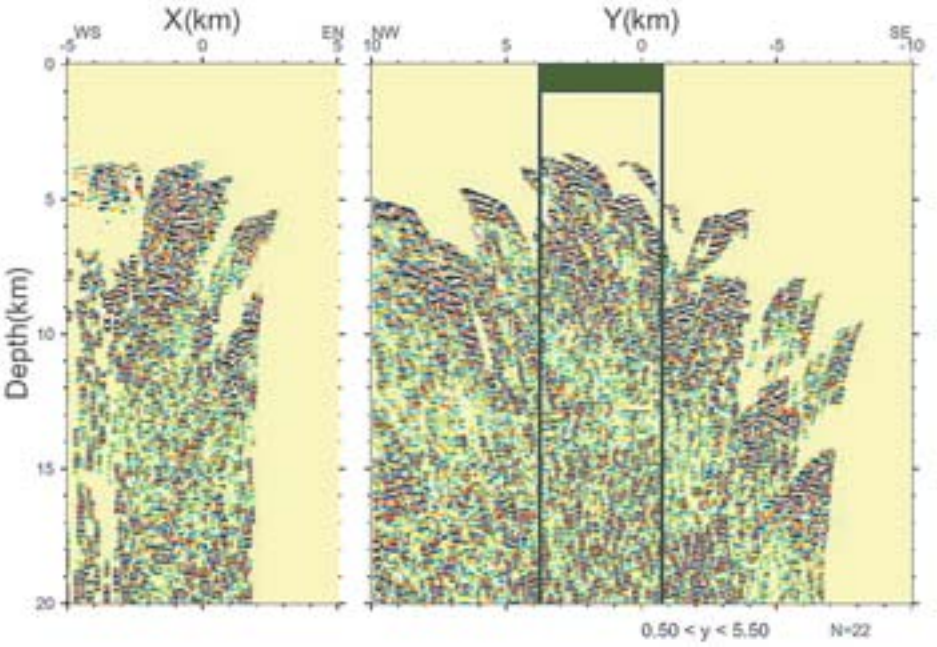

Fig. 4.26 NERP reflection profile along (Y) and across (X) the fault.

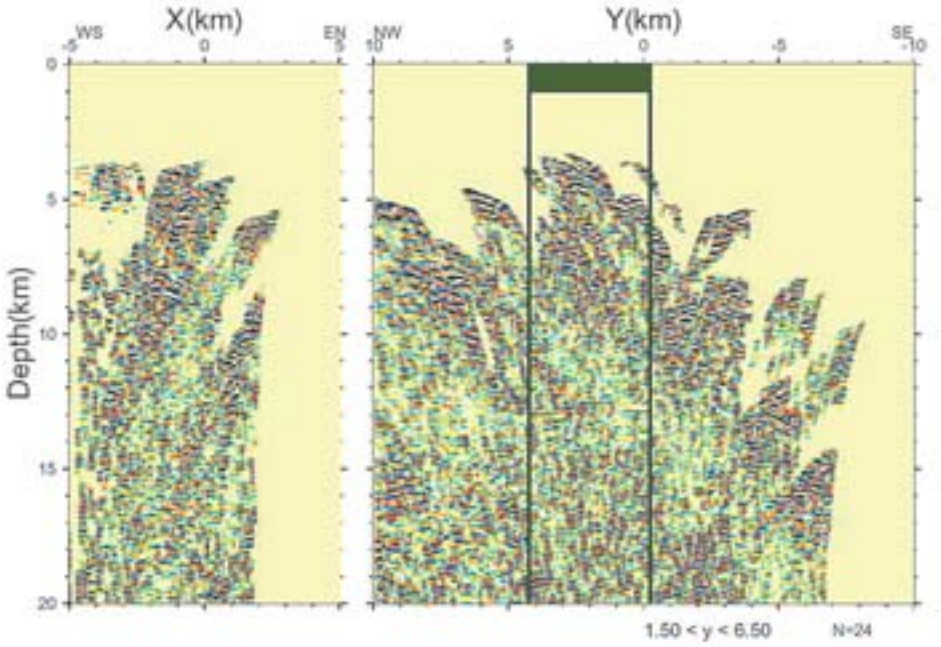

Fig. 4.27 NERP reflection profile along (Y) and across (X) the fault.

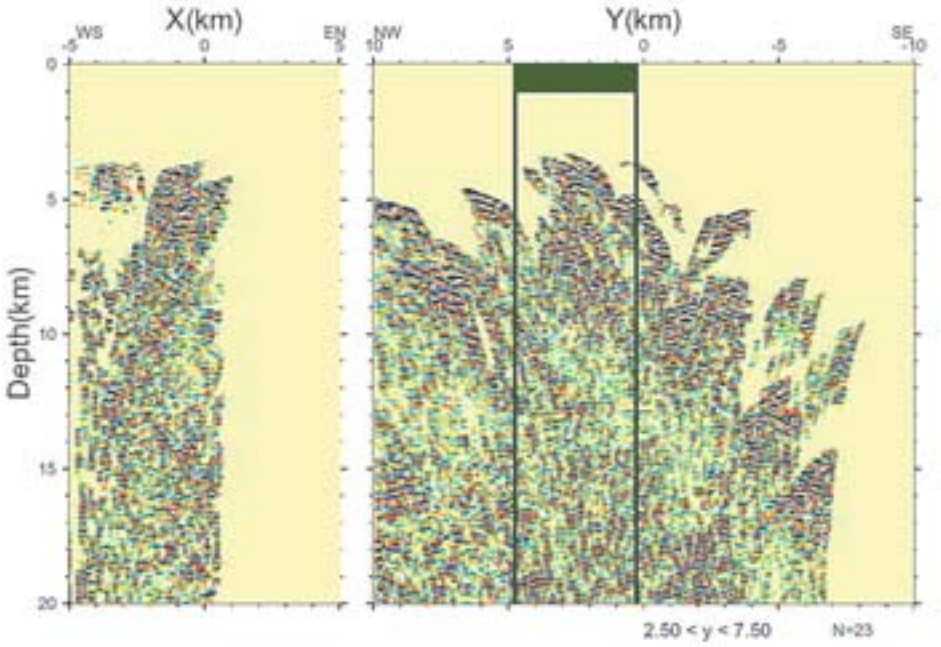

Fig. 4.28 NERP reflection profile along (Y) and across (X) the fault.

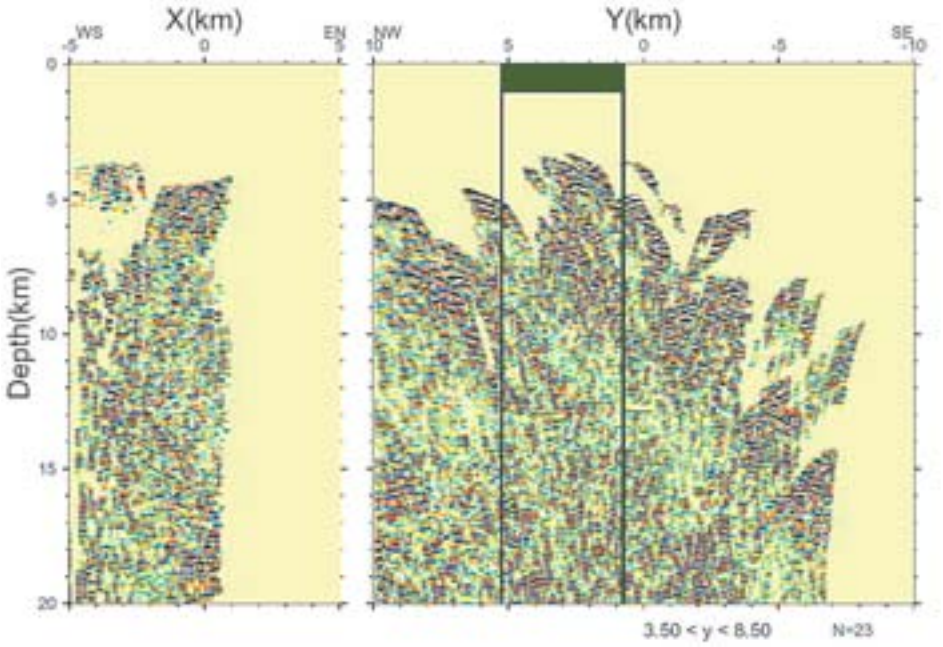

Fig. 4.29 NERP reflection profile along (Y) and across (X) the fault.

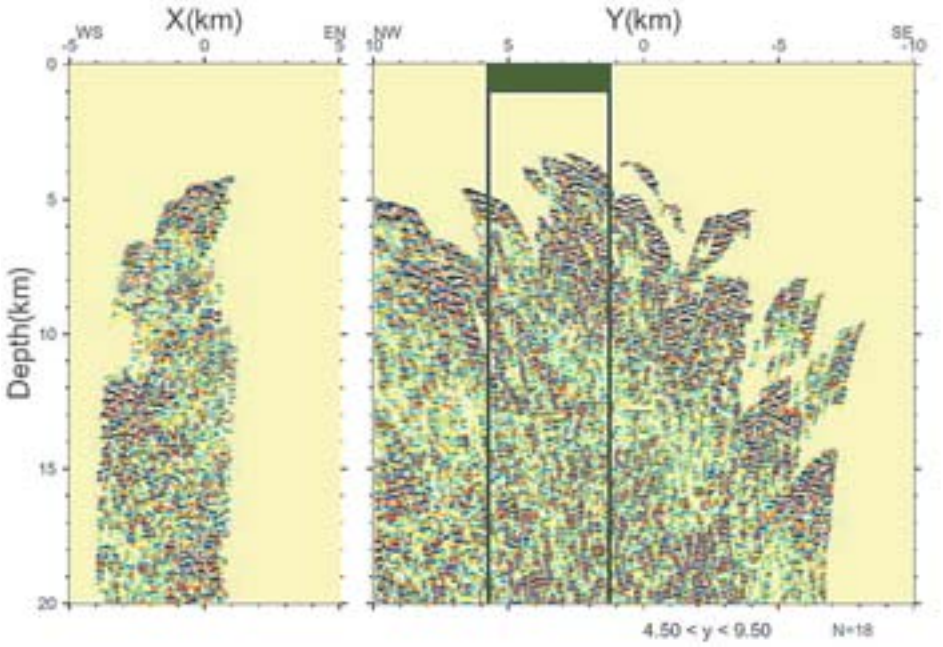

Fig. 4.30 NERP reflection profile along (Y) and across (X) the fault.

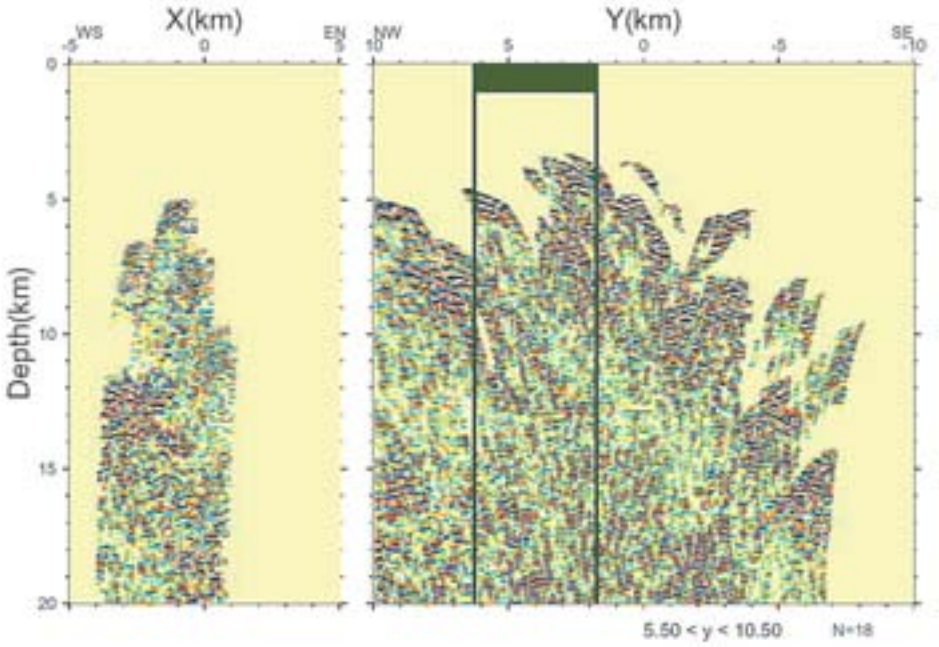

Fig. 4.31 NERP reflection profile along (Y) and across (X) the fault.

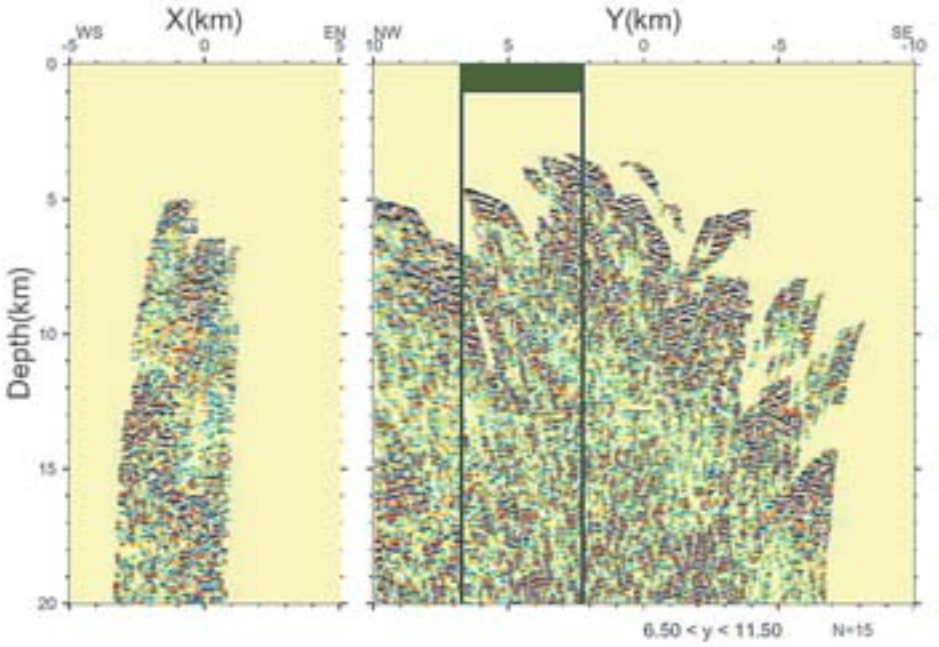

Fig. 4.32 NERP reflection profile along (Y) and across (X) the fault.

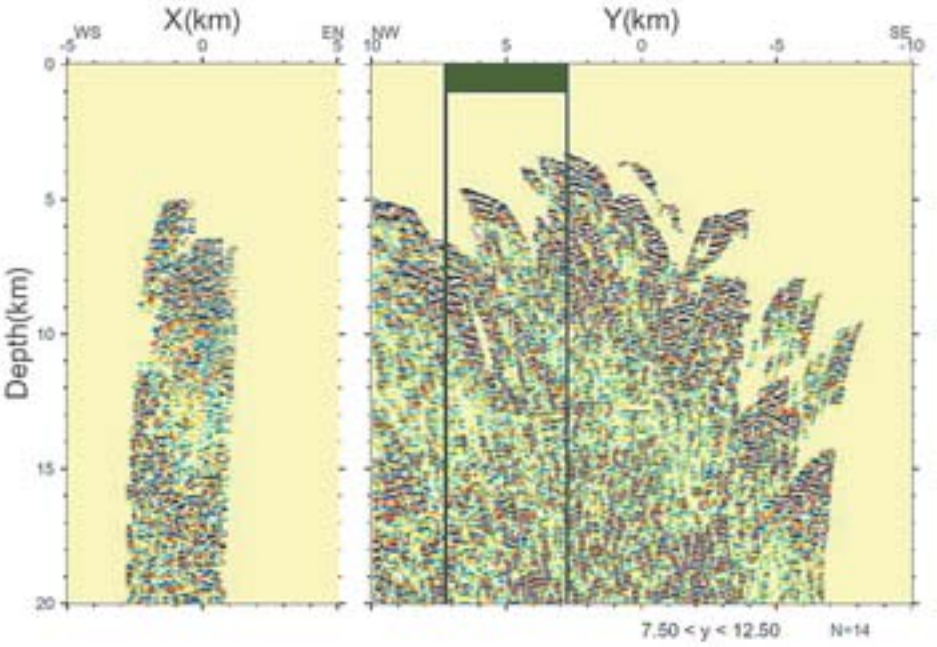

Fig. 4.33 NERP reflection profile along (Y) and across (X) the fault.

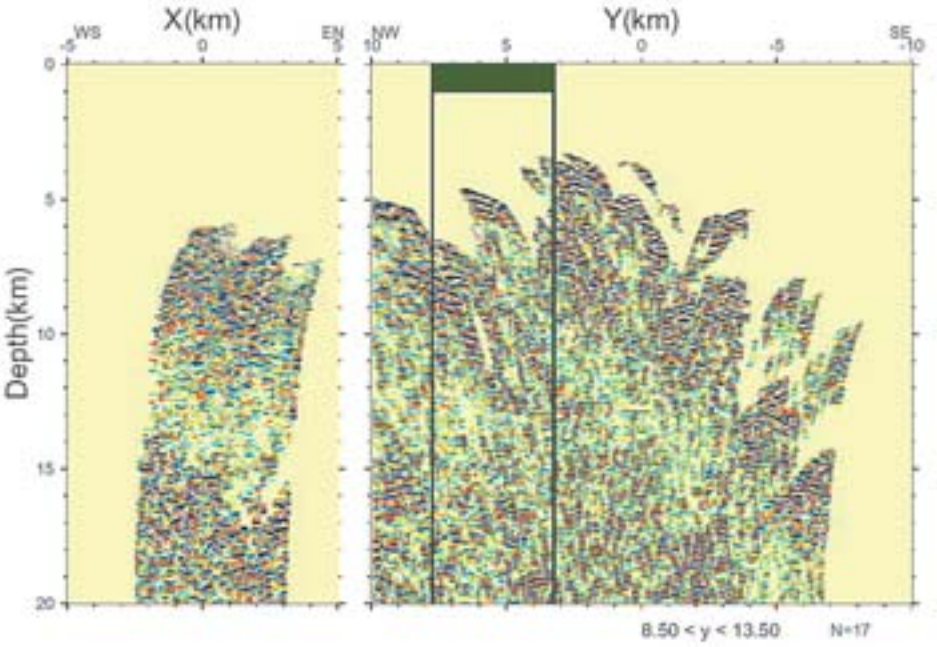

Fig. 4.34 NERP reflection profile along (Y) and across (X) the fault.

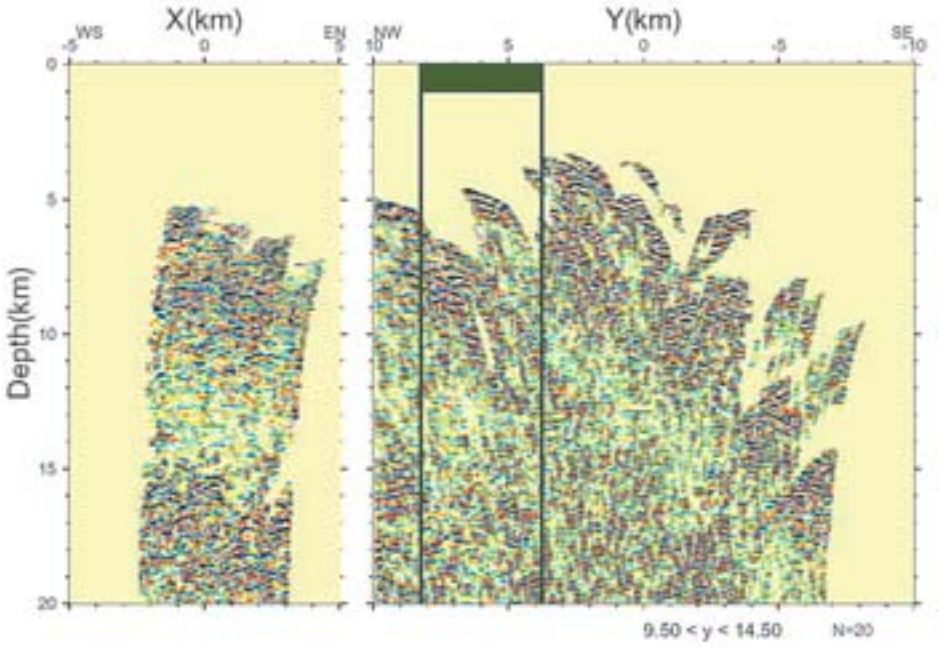

Fig. 4.35 NERP reflection profile along (Y) and across (X) the fault.

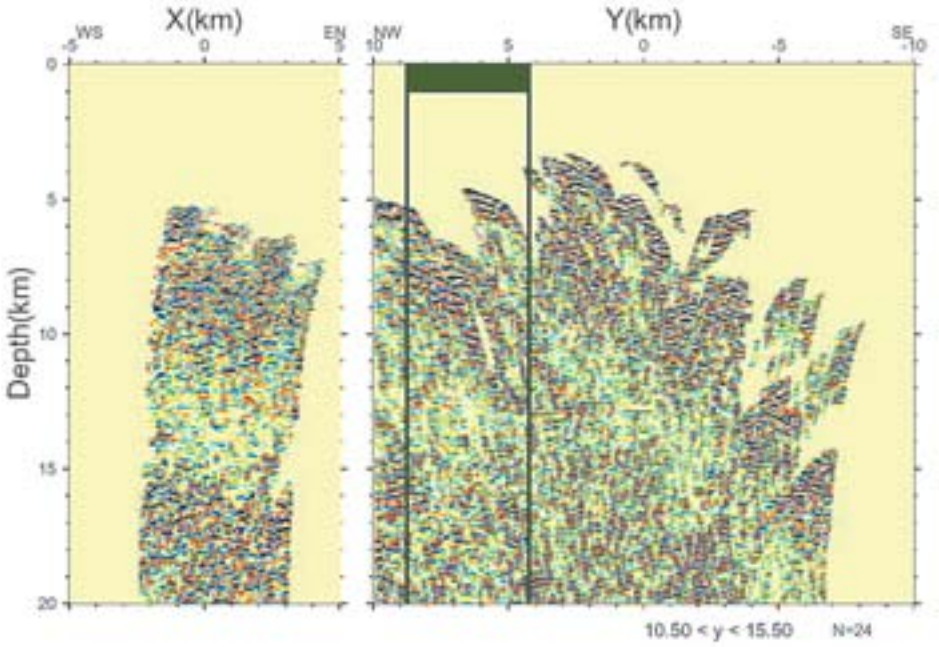

Fig. 4.36 NERP reflection profile along (Y) and across (X) the fault.

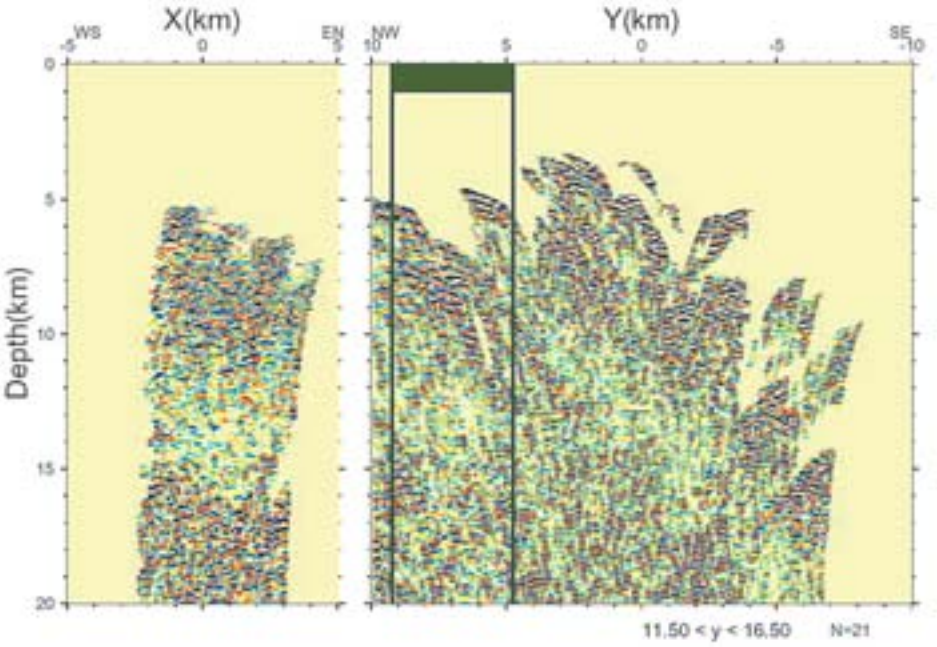

Fig. 4.37 NERP reflection profile along (Y) and across (X) the fault.

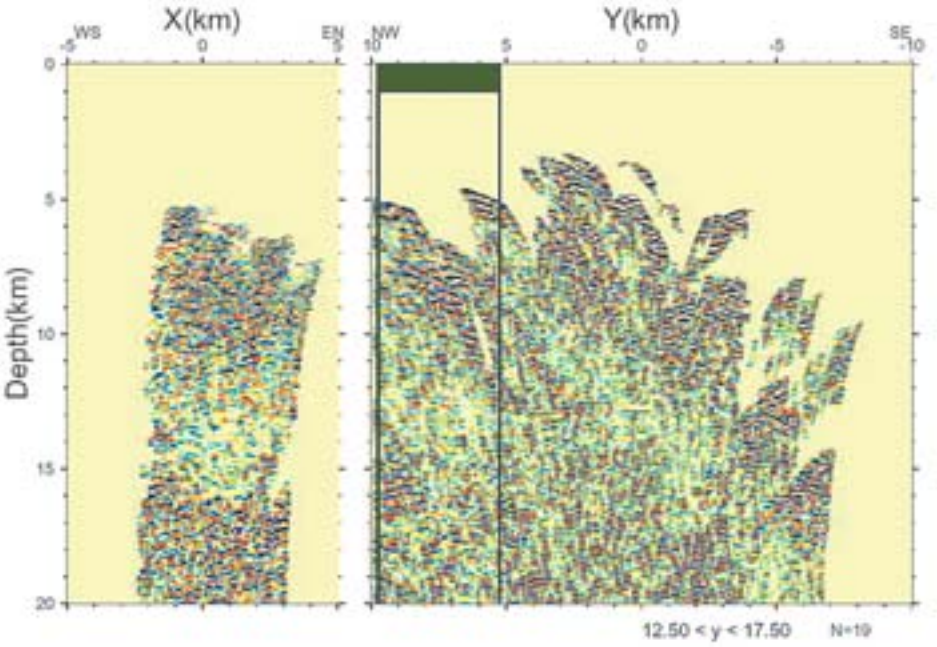

Fig. 4.38 NERP reflection profile along (Y) and across (X) the fault.

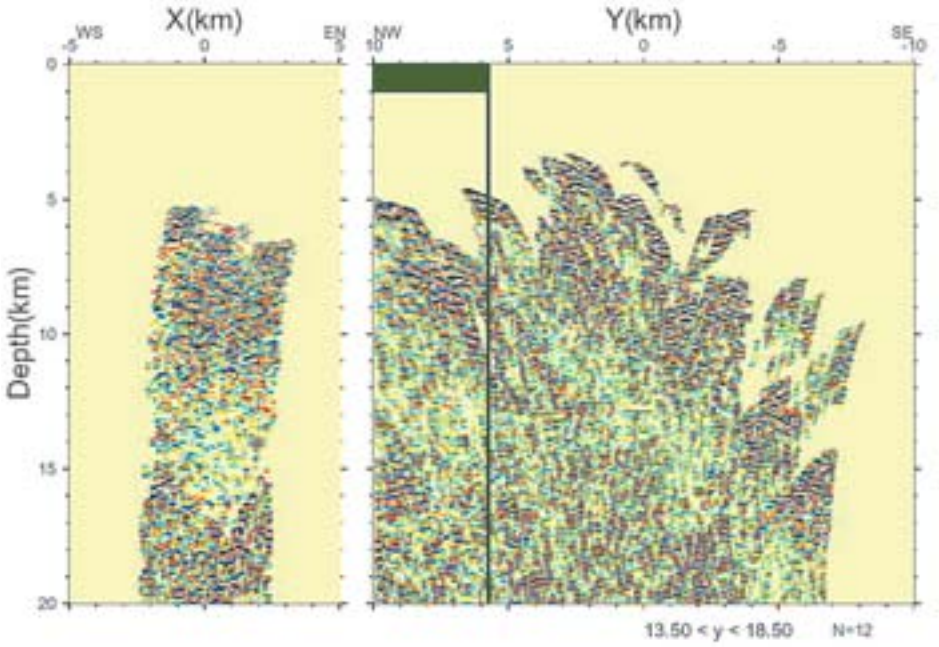

Fig. 4.39 NERP reflection profile along (Y) and across (X) the fault.

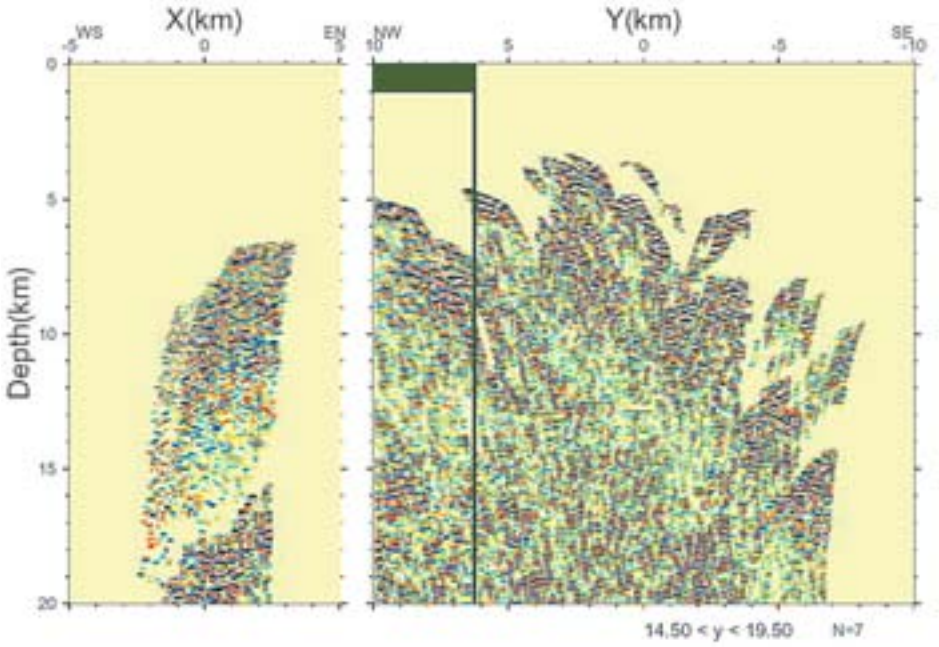

Fig. 4.40 NERP reflection profile along (Y) and across (X) the fault.

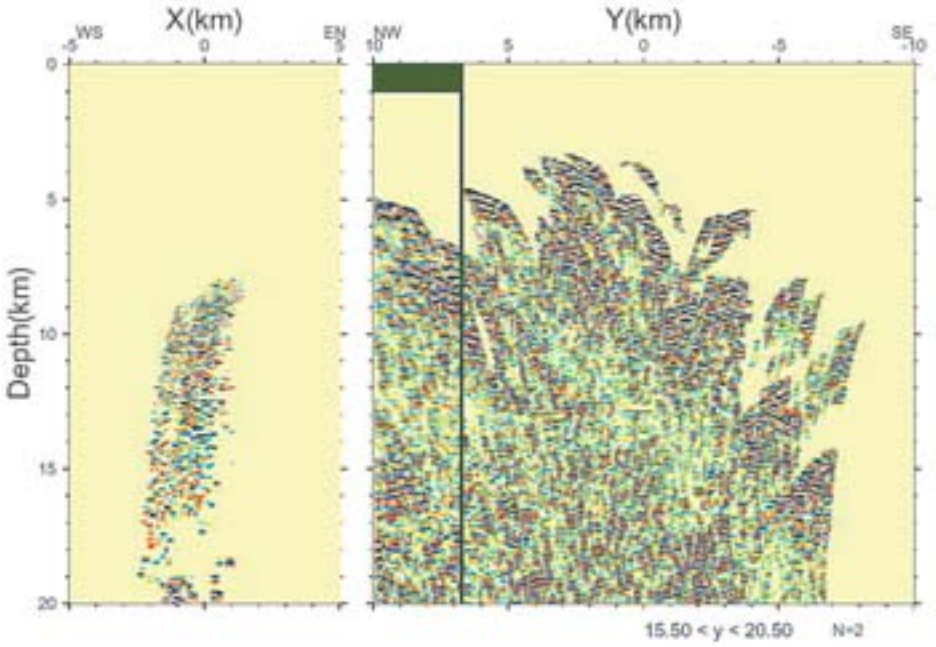

Fig. 4.41 NERP reflection profile along (Y) and across (X) the fault.

5. Discussion

5.1 Relationship between aftershock distributions and reflectors

Fig. 5.1 shows comparison between the NERP profile and the aftershock distribution (Chiba *et al*., 2003). Between depths of 5 and 9 km, several reflectors are found and the aftershock distribution is diffused three dimensionally. Between depths of 9 and 14 km, reflectors are not clearly seen and the aftershocks are concentrated near a plane, which is suggested to be the fault plane of the main shock. The area where aftershocks occurred has several reflectors.

5.2 Relationship between scatterer distribution and reflectors

Fig. 5.2 shows a comparison between the NERP profile and scatterer distribution (Kawamura *et al*., 2003). In the region between depths of 5 and 9 km, P-wave scatterers are also distributed. The reflector at a depth of 9 km is the bottom of the scatterer distributions.

The surface geology of this area suggests the intrusive granite is distributed in the studied area (**Fig. 5.3**). Kawamura *et al*. (2003) suggests that the scatterers are distributed in this intrusive granite (**Fig. 5.4**). In the Sangun metamorphic rocks, which are basement rock, under this intrusive granite, no scatterers are found (**Fig. 5.4**). The reflector at a depth of 9 km corresponds to the boundary between the intrusive granite and the Sangun metamorphic rocks.

The region between depths of 5 and 9 km has three characteristics, (1) several reflectors are visible in the NERP profile (**Figs. 4.17-4.41**), (2) the *P*-wave scatterers are distributed (**Fig. 5.4**), and (3) the aftershock distribution is diffused three dimensionally (**Fig. 5.1**). The heterogeneity of this region is high.

5.3 The less-reflective zone in a depth range between 5 and 9 km

In an area between depths of 5 and 9 km, some less-reflective zones, hereafter referred to as blank zone, are found (**Fig 5.5**). The definition of blank zones is the region in which the reflectors are not clearly found compared with the vicinity. The size of each blank zone is 1 – 2 km in horizontal dimension and 3 – 4 km in depth dimension.

Compared with the aftershock distribution, no aftershocks are distributed in these blank zones (**Fig. 5.6**).

In **Fig. 5.7**, slip distribution of the main shock (Iwata and Sekiguchi, 2002) is overlaid on **Fig. 5.6**. The slip of the main shock in these blank zones is very low.

Swarm-like seismic activities occurred in 1989, 1990 and 1997 in the same area as the 2000 western Tottori Prefecture earthquake. Shibutani *et al*. (2002) relocated the hypocenters. They indicated that those three preceding swarms occurred in different parts of the same fault plane as the 2000 western Tottori Prefecture earthquake. I compare the NERP profiles with the hypocenter distributions of preceding swarms. No earthquake occurred in the blank zone (**Fig. 5.8**).

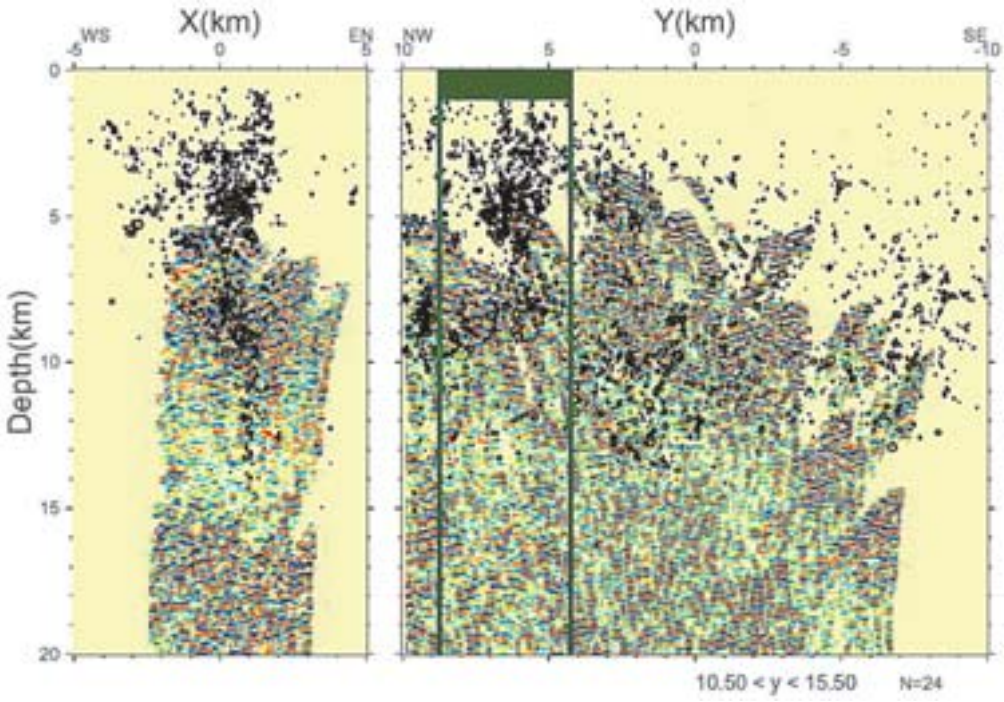

Fig. 5.1 NERP reflection profile and aftershock distribution.

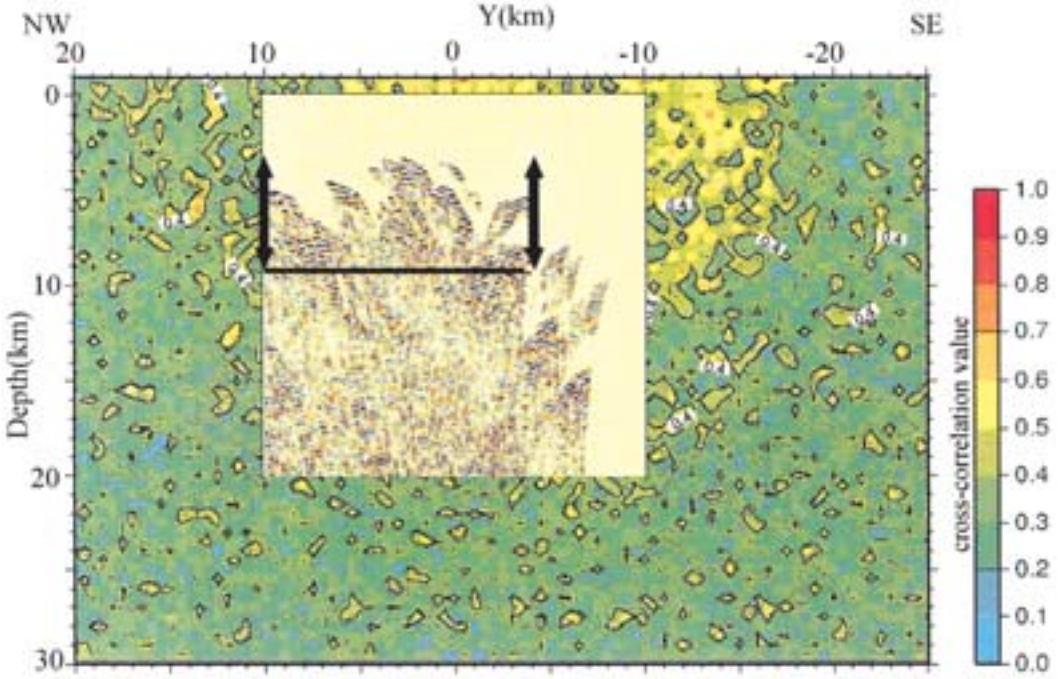

Fig. 5.2 NERP reflection profile and scatterer distribution (after Kawamura *et al*., 2003).

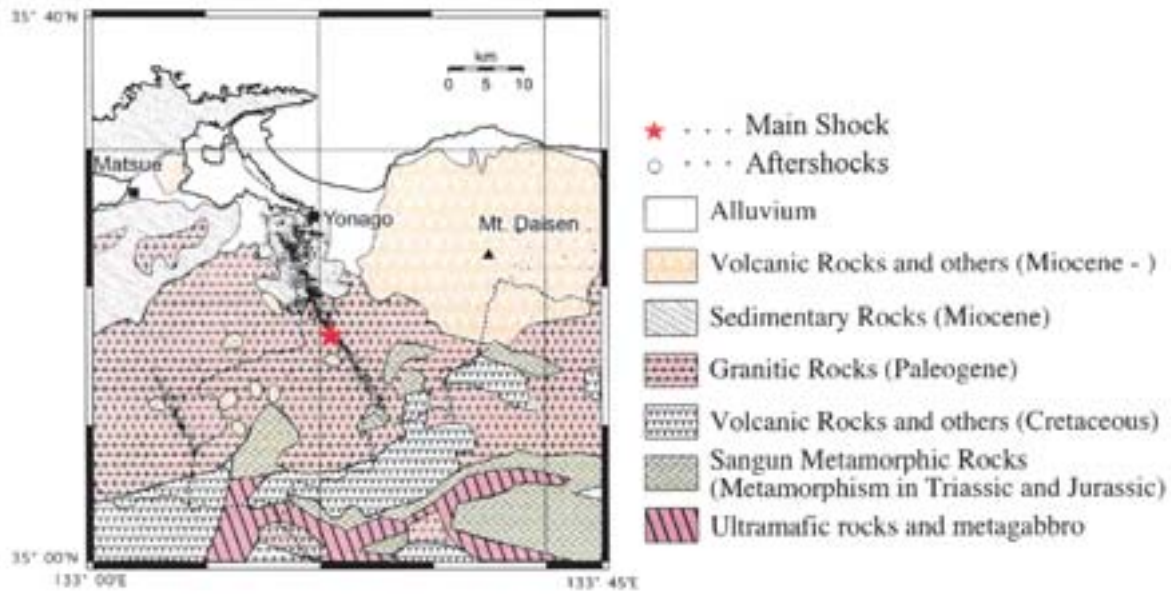

Fig. 5.3 Generalized geological map of the source region of the 2000 Western Tottori Prefecture earthquake (Kawamura *et al*., 2003).

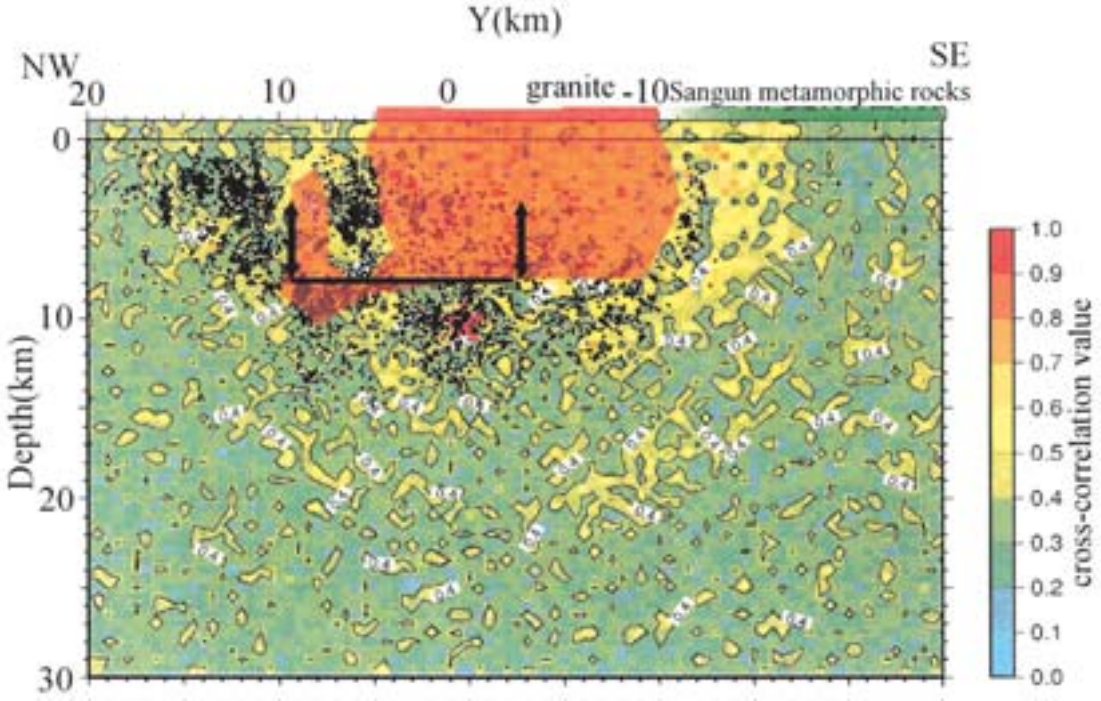

Fig. 5.4 Reflector at the depth of 9 km and scatterer distribution. The reflector is the boundary between the intrusive granite and basement rock (after Kawamura *et al*., 2003).

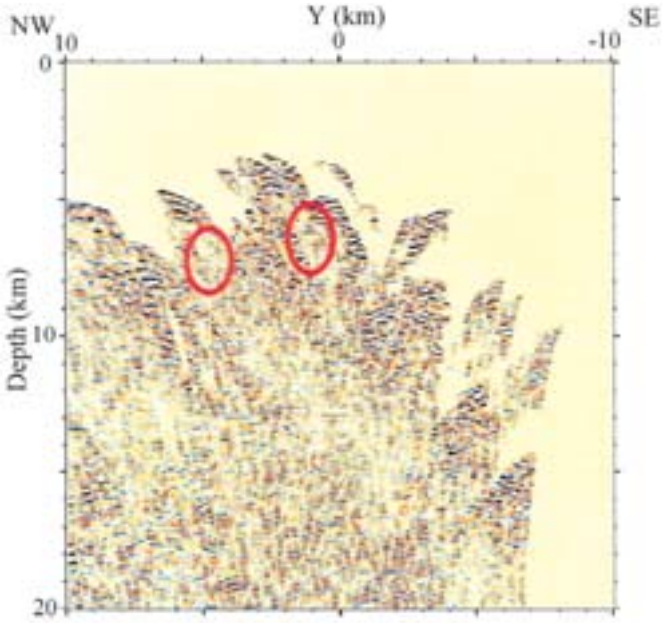

Fig. 5.5 Final NERP reflection profile along the fault. Red circles indicate the blank (less reflective) zones.

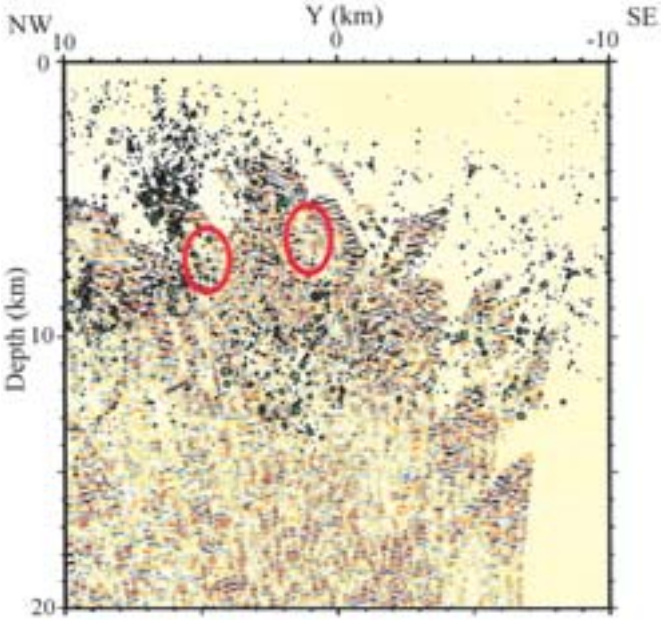

Fig. 5.6 Comparison between the blank (less reflective) zones and the aftershock distribution. Green circles indicate the aftershock distribution.

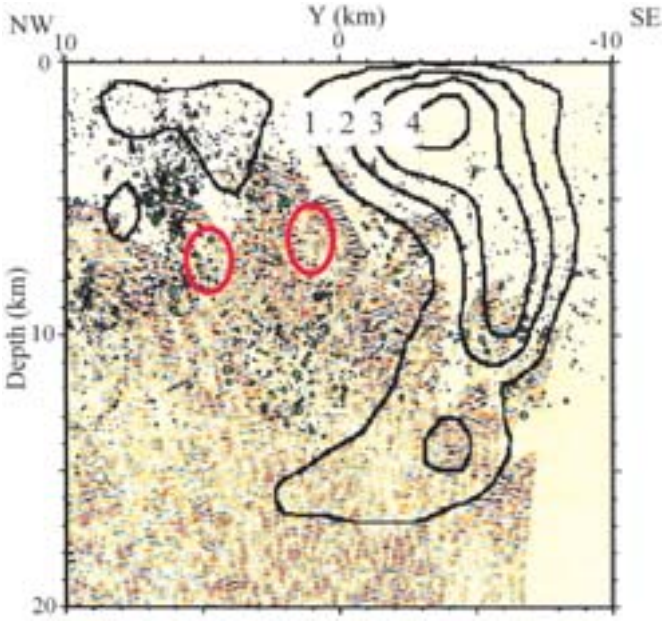

Fig. 5.7 Comparison between the blank (less reflective) zones and the slip of main shock (black contours) (Iwata and Sekiguchi, 2001).

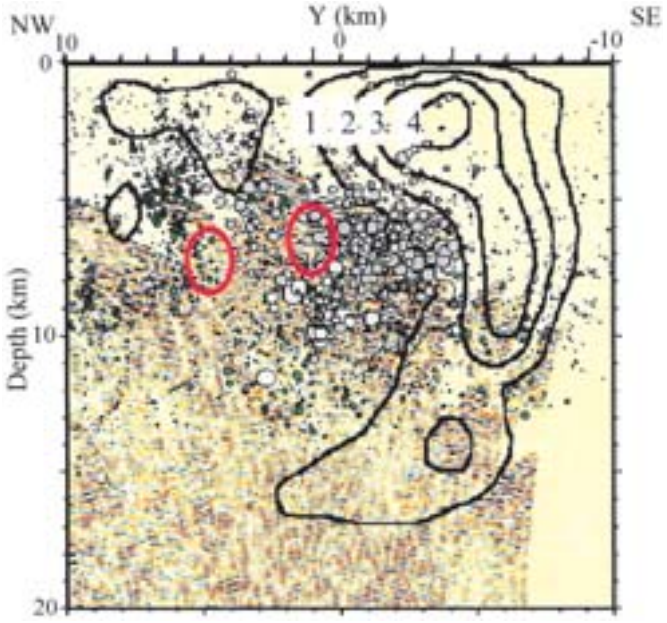

Fig. 5.8 Comparison between the blank (less reflective) zones and the swarm-like seismic activities (gray circles) (Shibutani *et al*., 2002).

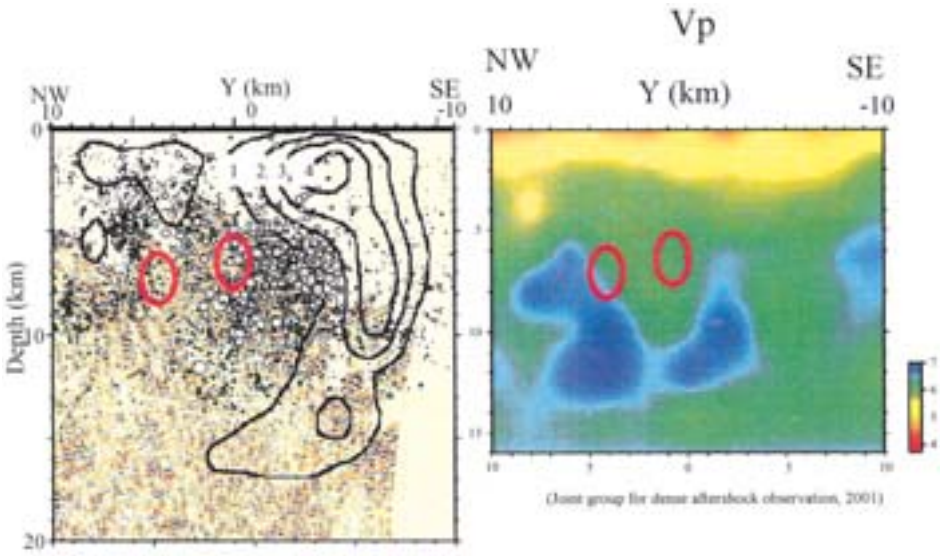

Fig. 5.9 Comparison between the blank (less reflective) zones and the P wave velocity.

Finally, I compare the profile with the *P* wave velocity structure (Joint Group for Dense Aftershock Observation, 2001). The *P* wave velocity of the blank zone is slightly lower than those in the neighbor area (**Fig. 5.9**).

All of the characteristics of the blank zones indicate that the blank zone, which is less-reflective zone, is not brittle fracture but stably slip area. It is possible that the stable slip areas are sprinkled in the upper crust, which may contribute to mechanism that no distinctive surface deformation occurred on the surface.

6. Conclusions

The aftershock observations were conducted in the source region of the 2000 western Tottori prefecture earthquake. I participated in two aftershock observations. One is a multi-channel aftershock observation. A multi-channel seismic array was deployed along and across the main fault area. The multi-channel array was operated for 85 hours to obtain quasi-continuous records of aftershocks. Two hundred and ninety-six events were recorded in the multi-channel array. To exclude the noisy events, I manually checked all the traces of recorded events (about 70,000 traces). I selected 81 events among them as good for analyzing.

The other observation is a very dense aftershock observation carried out by the Joint Group for Dense Aftershock Observation. Fifty-seven temporary stations were deployed in and around the source region. I used these aftershock data to image the crustal structure in this study.

Widely used method to image the heterogeneous crustal structure is the common midpoint (CMP) reflection method. The sources and receivers are located at or near the surface in the CMP method.

Since the natural earthquakes are not located on the surface of the earth, I cannot use the usual CMP method. Therefore, I proposed a new method, the natural earthquake reflection profiling (NERP) method, to image the crust using natural earthquakes. This method strongly depends on the hypocentral location and origin time of earthquakes and the background velocity structure. To estimate these unknown parameters, the Joint Hypocenter Determination (JHD) method was applied.

Then, I applied the NERP method to the data by assuming both *PP* and *SS* reflections. Since both *PP* and *SS* profiles image the reflectors at the same depth, I can interpret that the reflectors are not the ghost reflection due to converted waves but the real reflectors. The results are as follows. Above a depth of 5 km, no image is found because of few aftershocks in shallow depth. In the depth range from 5 to 9 km, several reflectors are visible. Between 9 and 14 km depth, the reflectors are not clearly found. Below a depth of 14 km, many reflectors are visible.

At depths between 5 and 9 km, the aftershocks are diffused three dimensionally. But, at depths between 9 and 14 km, the aftershocks are concentrated around the fault plane. The area, in which the aftershocks are diffused three dimensionally, is reflective, and vice versa.

At depths between 5 and 9 km are *P* wave scatterers distributed. The reflector at a depth of 9 km corresponds to the bottom of the scatterer distributions. The surface geology of this area is intrusive granite, and the scatterers are distributed in this intrusive granite. The reflector at the depth of 9 km is

corresponding to the boundary between the intrusive granite and the basement rock.

At depths between 5 and 9 km, some less-reflective zones (blank zones) are found. Compared with the aftershock distribution, no aftershocks occurred in the blank zones. A very small slip occurred on the fault plane during the main shock in the blank zones. Compared with recent swarm-like seismic activities in 1989, 1990 and 1997, no earthquake occurred in the blank zones. The *P* wave velocity in the blank zones is slightly slower than those in the neighbor areas. Those characteristics of the blank zones indicate that the blank less-reflective zone is not brittle fracture but stably slip area. It is possible that the stable slip areas are sprinkled in the upper crust, which may contribute to the major characteristics of the 2000 western Tottori Prefecture earthquakes.

Acknowledgements

We would like to thank all of the members of the Japanese university group of the MCS array aftershock observation for the data acquisition. We would also like to thank Prof. Naoshi Hirata, Prof. Hiroshi Sato, Dr. Tomonori Kawamura and Dr. Eiji Kurashimo for their numerous valuable comments, and the Japan Meteorological Agency for providing the hypocenters. We used GMT software [Wessel and Smith, 1991] to draw the figures.

References

1) Abe, S., Miyakoshi, K., and Inoue, D. (2001): Seismic Reflection Survey around the 2000 Tottori-ken Seibu Earthquake area, Abstracts 2001 Japan Earth and Planetary Science Joint Meeting, S3-P013.
2) Chiba, M., Hirata, N., Urabe, T., Kawamura, T., Nakagawa, S., and Kurashimo, E. (2003): Detailed aftershock distribution of the 2000 Tottori-ken Seibu Earthquake, Abstracts 2003 Japan Earth and Planetary Science Joint Meeting, S045-005.
3) Dillon, P. B. and Thomson, R. C. (1984): Offset Source VSP Surveys and their Image Reconstruction, Geophysical Prospecting, **32**, 790-811.
4) Fukuyama, E., Ellsworth, W. L., Waldhauser, F., and Kubo, A. (2003): Detailed Fault Structure of the 2000 Western Tottori, Japan, Earthquake, Bull. Seism. Soc. Am., **93**, 1468-1478.
5) Geographical Survey Institute (2001): Crustal movements in the Chugoku district, Rep. Coord. Comm. Earthq. Predict. **65**, 592-618 (in Japanese).
6) Hirata, N. and Matsu'ura, M. (1987): Maximum-likelihood estimation of hypocenter with origin time eliminated using non-linear inversion technique, Phys. Earth Planet. Inter., **47**, 50-61.
7) Iwaki, Y., Hashida, I., Tada, M., Ikawa, T., and Yagi, A. (1991): Highly Efficient Multi-Channel Geophysical Data Acquisition System, Butsuri-Tansa, **44**, 232-240.
8) Iwata, T. and Sekiguchi, H. (2002): Source inversion of recent earthquakes using strong motion records, in a special issue on Strong Motion Prediction, Chikyu Monthly, **37**, 47-55 (in Japanese).
9) Joint Group for Dense Aftershock Observation (2001): Very Dense Aftershock Observation of the 2000 Tottori-ken Seibu Earthquake (MJMA = 7.3) in the Southwestern Honshu, Japan – Aftershock Distribution, Focal Mechanisms, 3-D Structure in the Source Region and Their Relationship to the Source Process, Eos Trans. AGU, **82**(47), Fall Meet. Suppl., Abstract S41A-0595.
10) Kawamura, T., Nakagawa, S., Chiba, M., Kurashimo, E., Sato, H., and Hirata, N. (2003): Imaging of P-wave scatterer near the aftershock area of the Tottori-ken Seibu Earthquake, Japan, Abstracts 2003 Japan Earth and Planetary Science Joint Meeting, S053-003.
11) Kissling, E., Ellsworth, W. L., Eberhand-Phillips, D., and Kradolfer, U. (1994): initial reference models in local earthquake tomography, J. Geophys. Res., **99**, 19635-19646.
12) Kurashimo, E., Nakagawa, S., Kasahara, K., Nishida, R., Umeda, Y., Katsumata, K., Hasegawa, A., Hirata, N., and The Joint Group for Dense Aftershock Observation of the 2000 Tottori-ken Seibu Earthquake (2001): Seismic imaging in the focal region of the 2000 Tottori-ken Seibu Earthquake using Vibrators, Abstracts 2001 Japan Earth and Planetary Science Joint Meeting, S3-P012.
13) Matsumoto, S., Obara, K., Kimura, N., and Nakamura, M. (2002): Imaging P-wave Scatterer Distribution around the Focal Area of the 2000 Western Tottori Earthquake (Mw 6.6), Zishin, **55**, 229-232 (in Japanese).
14) Nishida, R., Hirata, N., Ito, K., Umeda, Y., Ikawa, T., and Onishi, M. (2002): Underground Structure Investigation in Western Tottori Prefecture (Part 1), Program. Abst., Seism. Soc. Jpn., P062 (in Japanese).
15) Scales, J. A. (1995): Theory of Seismic Imaging, Lecture Notes in Earth Sciences, **55**, 291 pp., springer-Verlag Berlin Heidelberg.
16) Shibutani, T., Nakao, S., Nishida, R., Takeuchi, F., Watanabe, K., and Umeda, Y. (2002): Swarm-like seismic activity in 1989, 1990 and 1997 preceding the 2000 Western Tottori Earthquake, Earth Planets space, **54**, 831-845.
17) Urabe, T. (1994): A common format for multi-channel earthquake waveform data, Program. Abst., Seism. Soc. Jpn., 384p (in Japanese).
18) Waldhauser, F. and Ellsworth, W. L. (2000): A double-difference earthquake location algorithm: Method and application to the Northern Hayward Fault, California, Bull. Seism. Soc. Am., **90**, 1353-1368.
19) Wessel, P. and Smith, W. H. F. (1991): Free software helps map and display data, Eos Trans. AGU, **72**, 441, 445-446.

(Accepted : April 4, 2005)

Appendix

We used data acquired by the Japanese University Group of the MCS Array Aftershock Observation of the 2000 Western Tottori Prefecture earthquake, participants of which include Shin Koshiya, Akimasa Abumi (Iwate University); Tanio Ito, Takahiro Miyauchi, Tomonori Kawamura, Katsuko Suzuki (Chiba University); Hiroshi Sato, Takaya Iwasaki, Naoshi Hirata, Eiji Kurashimo, Yoichiro Ichinose, Mamoru Saka, Sumiko Ogino, Shigeki Nakagawa, Keiji Adachi, Naoko Kato, Satoru Nagai (the University of Tokyo); Miho Chiba (Tokyo University of Science); Ryohei Nishida, Hirofumi Nishiyama, Takafumi Yoden, Wataru Munafuji (Tottori University); Akira Yamada, Takashi Ushio (Okayama University); Shuichiro Yokota, Tsuyoshi Sakurai, Mihoko Sonobe, Miwa Akashi (Shimane University); Takeshi Ikawa, Yoshio Kawabe, Toru Kuroda (JGI Inc.).

Report of the National Research Institute for Earth Science and Disaster Prevention, No.68; September, 2005

2000年鳥取県西部地震の余震を用いた地殻のイメージング

中川茂樹

独立行政法人　防災科学技術研究所　固体地球研究部門
（現：東京大学地震研究所　地震予知情報センター）

要　旨

2000 年 10 月 6 日に鳥取県西部を震源とする M(JMA) 7.3 の地震が発生した．この地域の震源断層付近の地殻不均質構造を明らかにするために，多チャンネル地震計アレイを使った余震観測を行った．従来の制御震源を用いた共通反射点重合法（CMP 法）では，地表に震源と観測点をアレイ状に並べ，それらの共通中点で反射する波を NMO 補正して重合し地下のイメージを得ている．しかし，自然地震の場合は震源が地下深くにあるので，反射点は震源と観測点の中点にはない．そこで本研究では，新たに開発した「自然地震反射法」を用いて従来の制御震源地震探査では得られなかった地殻のイメージを得ることを目的とした．解析の結果得られた反射面の分布と余震分布などを比較したところ，以下のような特徴が得られた．1）深さ 5-9 km には反射面が多く見られ，余震が 3 次元的に分布しており，不均質性が大きい．2）深さ 9-14 km には反射面が少なく，余震は面的に分布しており，比較的均質である．3）深さ 14 km 以深には反射面が多く見られるが，余震は分布せず，不均質性は大きい．4）上部地殻に脆性破壊しない領域のあることが示唆された．

キーワード：余震観測，地殻構造，2000 年鳥取県西部地震